4-19-2011

A Study on The Use of Double Helix Point Spread Functions in 3D Fluorescence Microscopy

Sreya Ghosh

To the University Council:

The Thesis Committee for Sreya Ghosh certifies this is the final approved version of the electronic thesis: “A Study on The Effect of Double Helix Point Spread Function on 3D Fluorescence Microscopy”.

_____

Chrysanthe Preza, D.Sc.

We have read this thesis and
recommend its acceptance:

_____

Eddie L. Jacobs, D.Sc.

_____

Aaron L Robinson, Ph.D.

Accepted for the Council:

_____

Karen D. Weddle-West, Ph.D.
Vice-Provost for Graduate Programs

A STUDY ON THE USE OF DOUBLE-HELIX POINT SPREAD FUNCTIONS IN 3D FLUORESCENCE MICROSCOPY

by

Sreya Ghosh

A Thesis

Submitted in Partial Fulfillment of the

Requirements for the Degree of

Master of Science

Major: Electrical and Computer Engineering

The University of Memphis

May, 2011

This thesis is dedicated to my mother Saswati Sen *and grandmothers* Karuna Sen *and* Rama Ghosh *for their never ending sacrifices*.

Acknowledgements

I would first like to thank Dr. Chrysanthe Preza, for her constant support, patience, motivation, enthusiasm and help during the writing of this thesis. I am extremely grateful to have her as my advisor, and much more.

I am grateful to Dr. Eddie Jacobs and Dr. Aaron L. Robinson who devoted their precious time for being in my thesis committee and for the valuable suggestions. I would also like to thank Dr. Rama Prasanna Pavani, Ginni Sharma, Sean Quirin and Dr. Rafael Piestun at the University of Colorado for all their advice and help during the work for this thesis and helping me to understand their work. I would like to thank Dr. Shuai Yuan for his advice throughout the writing of this thesis.

I would also like to thank my lab mates Mark Sporrer, Karthika Muthukuri at the CIRL for their suggestions during my research.

Lastly, I would like to thank my family and friends for their constant support and encouragement.

Abstract

Ghosh,S. M.S. The University of Memphis. 2011. Study on: The Effect of Double-Helix Point Spread Functions on 3D Fluorescence Microscopy. Dr. Chrysanthe Preza:

Noninvasive three-dimensional (3D) imaging of thick samples in fluorescence microscopy is traditionally achieved via the method of optical sectioning which requires multiple two-dimensional images of an object acquired while focusing at different depths within the object. Defocus, spherical aberrations (SA) and photo bleaching are known to affect the accuracy achieved in 3D images. Double-Helix point spread functions (DH-PSF), the result of PSF engineering, have been used for super localization of point sources in 3D samples. The unique DH-PSF design features 2 dominant lobes in the image plane which appear to rotate as the axial (z) position of a point light source with respect to the imaging lens is changed. Thus, the angular orientation of the DH-PSF lobes encodes the imaging depth. The DH-PSF lobes are horizontal when the emitter is in focus. As the emitter is moved toward the objective lens, the DH-PSF lobes rotate, however, if the emitter is moved away from the objective the lobes rotate in the opposite direction. In this thesis, the effect of the DH-PSF in 3D optical sectioning microscopy is studied for different imaging conditions using simulations that introduce SA and noise. The frequency domain features of the DH-PSF were studied and were shown to preserve the rotation characteristic that encodes depth information. In addition frequency analysis shows that the DH-PSFs are less sensitive to defocus and SA at small imaging depths than the conventional PSF. The effect of SA is shown to cause an error in the super localization of emitters which it was successfully corrected by a new methodology developed in this thesis. Different approaches to estimate intensity and location of

structures from computer generated images were investigated. The objects were effectively recovered from the images with and without SA and noise. Thus from this study we conclude that DH-PSF based systems can be effectively integrated into the conventional fluorescent microscopy system to help in particle tracking, super localization and object ranging.

Table of Contents

List of Figures

Figure **Page**

List of Abbreviations

3D: Three dimensional

2D: Two dimensional

ATF: Amplitude Transfer Function

CRB: Cramer-Rao Bound

COSI: Computational Optical Sensing and Imaging

COSMOS: Computational Optical Sectioning Microscopy-Open Source

DH-PSF: Double Helix Point Spread Functions

DVEM: Depth Variant Expectation Maximization

GL: Gauss- Laguerre

I-Div: I-Divergence

LLS: Linear Least Squares

L-MAP: Linear Maximum a Posteriori

MTF: Modulation Transfer Function

N.A.: Numerical Aperture

OTF: Optical Transfer Function

PSF: Point Spread Function

RI: Refractive Index

SA: Spherical Aberrations

SIEM: Space Invariant Expectation Maximization

SIM: Structured Illumination Microscopy

STED: Stimulated Emission Depletion Microscopy

1. Introduction

Fluorescence microscopy is one of the most popular three-dimensional (3D) imaging tools for biological studies. Noninvasive 3D imaging of thick samples in fluorescence microscopy is traditionally achieved via the method of optical sectioning which requires multiple two-dimensional (2D) images of an object acquired while focusing at different depths within the object [2]. The 2D images are stacked together to create a 3D volume representing the total image space. A 3D system is prone to the undesirable effects of defocus, spherical aberrations (SA), photo bleaching and loss of resolution. The point spread function (PSF) describes the response of an imaging system to a point source of light or point object i.e., it is the impulse response of the microscope system. With the development of faster and more accessible computers, raw data is obtained from the microscope and processed with algorithms to produce the best quality images [3].

With the advent of computational imaging, a method in which computers are used to process data from imaging systems such as the microscope, there has been a paradigm shift in microscopy. The new paradigm suggests that we can extract maximum information from the optical system by first making a change to the optical system which results in some intermediate image that needs processing in order to obtain the desirable image. The motivation behind this paradigm lay in obtaining an extended depth of focus [4], in extracting depth information [5] and overall improve imaging in ways that go beyond the conventional system capabilities. The system modification is also refer to as PSF engineering which involves altering of the pupil in a way that only relevant information is gathered at the imaging plane.

The double Helix point-spread function (DH-PSF) is the result of PSF engineering designed to yield super resolution microscopy [6].The DH-PSF design features two dominant lobes in the image plane which rotate with the change in axial (z) position of the light point source. The center of the DH-PSF gives the precise XY location of the point source, while the orientation of the lobes gives the axial location. In this thesis, the effect of the DH-PSF on computational optical sectioning microscopy in the presence of aberrations is investigated.

1.1. Aberrations in 3D Microscopy Image Formation

As the underlying object is moved away from focus, a blurry pattern is observed due to defocus. In 3D imaging, the 2D image at each focusing depth is contaminated by the effects of defocused projections from planes surrounding the infocus plane. The size of the airy pattern (i.e. the intensity of the jinc function) defines the resolution of the system and dictates how close two point objects can be brought together so that the system views them as distinctly different objects. In microscopes resolution is anisotropic, which means that axial resolution is worse than lateral resolution. Resolution beyond the resolution limit is known as super-resolution. Many techniques have been developed to achieve super-resolution like Structured Illumination Microscopy (SIM) [7], Stimulated Emission Depletions (STED) [8] and DH-PSF based systems [6].

Aberrations in imaging are primarily of 5 types: spherical aberration, coma, astigmatism, field curvature and chromatic aberration caused by refraction within the sample and the immersion medium of the objective lens, misalignment of the system,

curvature of the lens, and dispersion of light by the lens respectively [9]. Wide-field microscopes are corrected for most of these aberrations apart from spherical aberration. In 3D imaging with a conventional microscope systems depth-induced SA are particularly problematic when imaging thick samples.

1.1.1. Spherical Aberrations

A PSF due to a point source located anywhere in object space should be a linearly shifted version of the PSF due to a reference point source. In general, however, microscope systems are not shift invariant. In microscopy shift variance is traditionally divided into radial and axial shift variance. Spherical aberrations are an example of axial shift variance as discussed below.

Cells are often quite thick (5 to10 μm) and tissue slices are even thicker (> 10 μm) when compared with the depth of focus of a high-NA lens (0.2 μm) and have a refractive index closer to that of water (n = 1.33) than that of immersion oil (n = 1.515) used with most high-NA lenses. Under the design conditions, the object plane immediately below the coverslip is in focus at the design detector (camera) plane. For a point source located at some depth into the specimen layer to be observed, the stage containing the specimen must be shifted along the optical axis toward the lens until the desired object plane is in focus at the designed detector plane. The shift of the stage results in a decrease in the thickness of the immersion-oil layer separating the coverslip from the front element of the objective lens. For object points located deep in the specimen layer, light emitted by the observed object point must pass through layers whose thicknesses and refractive indices can vary significantly from the layers in the design system. The resulting optical

path length error causes the spherical aberration which in turn can severely degrade resolution and contrast of the 3D image [6].

Using the Gibson and Lanni [10] model to account for the aberrations under given imaging conditions, the intensity of the PSF at the back focal plane of the imaging lens is given by

$$I(x_d, y_d, z_d) = \left| \frac{C}{z_d} \int_0^1 J_0 \left[ka\rho \frac{({x_d}^2 + {y_d}^2)}{z_d} \right] e^{j\omega(\rho)} \rho d\rho \right|^2 \quad [1]$$

$I(x_d, y_d, z_d)$ is the intensity at location x_d, y_d, z_d in the 3 dimension respectively, where C is a constant complex amplitude. J_0 is the zeroth order Bessel function. Under the non-design conditions, the phase aberration $\omega(\rho)$ at the normalized radius ρ in the back focal plane is equal to the optical path length difference multiplied by the wave number $k=2\pi/\lambda$, where λ is the wavelength of the light emitted by the point source.

Light traveling through the layers of the specimen, coverslip and immersion medium suffers from refraction at every junction hence the total path length changes leading to aberrations which cause asymmetry and an apparent shift in the location of the object, which increases as we go deeper into the sample. The actual location of the object will be referred to as the true depth and the true depth summed with the apparent shift will be known as the apparent depth (Figure 1) throughout the rest of the thesis.

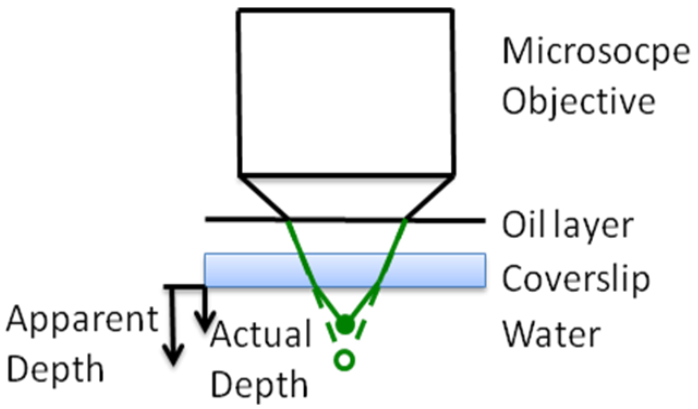

Figure 1. Effect of depth induced spherical aberrations on microscopy-based imaging.

1.2. Computational Imaging for Wide-field Microscopy

A wide-field (non-scanning, non-confocal) fluorescence microscope is one of the less expensive and widely used microscopes. Electron, confocal, scanning microscopes have improved imaging capabilities but still remain very expensive and less accessible. In an attempt to bridge the gap between improved images obtained from more expensive techniques and the cost effectiveness of conventional wide-field microscopes computational imaging plays a huge role. Additional benefits of the wide-field imaging approach are higher efficiency and throughput in collecting photons and the ability to account for SA computationally. Computational imaging applied to 3D fluorescence microscopy provides improved images by processing images acquired from wide-field microscopy using computational methods developed from model-based [3] algorithms.

1.2.1. 3D Deconvolution Algorithms to Improve Optical Sectioning

One of the earliest uses of computational imaging was to remove the effect of defocus from the images [11]. For a non-spherically aberrant system the system can be assumed

to have a single PSF, hence the system is called space invariant. Based on the assumption that the microscope is a space-invariant imaging system, 3D image formation has been modeled mathematically as the convolution of the 3D PSF of the system with the 3D intensity of the underlying object. Thus, using deconvolution techniques and a known PSF for the microscope, the processed image can give a better representation of the underlying object.

Unavoidably, processing leads to amplification of noise present in the measured images. Techniques based on regularization [12, 13] have been developed to minimize the effects of noise amplification.

The Computational Optical Sectioning Microscopy – Open Source (COSMOS) software developed at the Computational Imaging Research Lab (CIRL) at the University of Memphis [14], offers several algorithms for processing raw data acquired from a light microscope in order to obtain improved 3D imaging. 3D imaging results presented in this thesis were obtained using algorithms in the COSMOS software which we discuss in more detail below.

The COSMOS software package includes both non-iterative and iterative computational methods. The regularized linear least squares method (LLS) [13] and the linear maximum a posteriori (L-MAP) [15] are non-iterative and thus very fast. Iterative algorithms included in COSMOS such as the Jansson-van Cittert [11] and the Expectation Maximization algorithms are non-linear methods which have the capacity of using additional information such as positivity of fluorescence intensity, finite specimen support and specimen smoothness when solving the inverse imaging problem. Statistical

reconstruction takes into account randomness during image formation and image detection process. The Expectation Maximization (EM) algorithms [16, 17] derived to solve a maximum likelihood estimation problem based on Poisson statistics are particularly suitable for low-light fluorescence imaging. The space-invariant expectation maximization algorithm (SIEM) [17] and the depth-variant expectation maximization algorithm (DVEM) [16] were used throughout this thesis.

EM algorithms perform two main steps at each iteration: estimation and a maximization step. In the expectation step, the expected value of the log-likelihood function based on the given model and data is calculated, and in the maximization step, the value of the estimated parameters which maximize the likelihood is found [17]. Advantages of the EM algorithms include monotonic convergence to a global maximum and the positivity constraint is naturally enforced.

1.2.2. Correction for Depth-Induced SA using Computational Imaging

Most algorithms developed for de-blurring are based on the assumption of linearity and space invariance. In thick samples depth-induced SA is particularly significant aberration making system space invariance an invalid assumption. Preza and Conchello [16] suggested an efficient approach to correct SA in depth-variant imaging, in which the object space is divided into strata along the imaging depth. Each stratum is associated with the weighted interpolation of two PSFs, one defined at the top and the other at the bottom layer of the strata. Thus the number of depth-variant PSFs that account for the SA needed for the processing the data for de-blurring and correction of SA is kept at a minimum making the approach practical for use [18].

1.2.3. COSI Approach to Improve Performance of 3D Microscopy

Computational optical sectioning microscopy has revolutionized 3D imaging and it has opened the door to computational optical approaches that allow a great degree of freedom for the development of new techniques such as structured illumination microscopy (SIM) [7],cubic phase mask modified systems [4] or double helix mask modified systems [4] to name a few. These techniques are the result of a relatively new field known as Computational Optical Sensing and Imaging (COSI) which captures the development of computational optical systems based on an optimal approach that involves simultaneous development of computational methods matched to optics and opto-electronics to give a cohesive and high performance imaging system. The COSI approach gives the developer immense flexibility to develop systems based on joint optimization of these methods to obtain improved information content.

Rigorous frameworks for optimal joint design and performance of computational imaging systems have been presented [19-21]. Statistical approaches to quantify information content are based on the Fisher information measure and the Cramer-Rao bound (CRB). The ability to estimate a specific set of parameters, without regard to an unknown set of other parameters that influence the measured data, or nuisance parameters, is described by the Fisher Information matrix, and its inverse defined as the CRB [22]. The CRB is the lower bound, over all unbiased estimators, on the variance of the estimate of a parameter, given some data. The COSI approach has been applied to different areas in recent years [23] with successful examples in microscopy such as wave-front coding systems [4] and 3D imaging systems using engineered PSFs that are spatially rotating [5].

1.2.4. Point Spread Function Engineering

PSF engineering came into being with the desire to develop imaging systems with improved capabilities using the COSI approach. The motivation behind PSF engineering lies in improving the information content in the acquired images. PSF engineering involves altering of the pupil in a way that facilitates information retrieval relevant to an application to be gathered at the imaging plane in a form of an intermediate image. PSF engineering is achieved by introducing a phase mask in the back focal plane of the imaging lens to modulate the phase of the wavefront. Using appropriate computational methods the information can be efficiently extracted and the desired image can be restored from the intermediate.

Examples of PSF engineering based on wavefront encoding is the cubic phase mask PSF designed to extend the depth of field [5] and the double helix point-spread function (DH-PSF) which was designed to provide precise point location in microscopy [24].In this thesis we explore imaging with a modified microscope system characterized by an engineered DH-PSF, thus in what follows we discuss the DH-PSF in more detail.

1.2.5. Double Helix Point Spread Function (DH-PSF)

The DH-PSF design features 2 dominant lobes in the image plane whose angular orientation rotates with the axial (z) position of the emitter. The DH-PSF lobes are horizontal when the emitter is in focus. As the emitter is moved toward the objective lens, the DH-PSF lobes rotate, however, if the emitter is moved away from the objective the lobes rotate in the opposite direction.

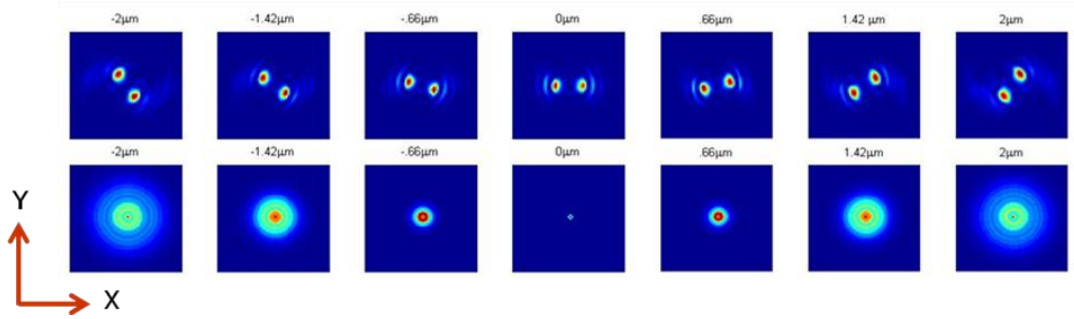

Figure 2. Comparison of 2D PSFs for a 0.45 N.A. lens with 633 nm wavelength computed at different depths of focus from -2.0 µm to 2.0 µm with best focus at 0 µm. **Top Row:** Conventional 2D PSF. **Bottom Row**: DH-PSF obtained from the conventional PSF using the implementation procedure described in (Figure 6).

In effect, the PSF appears as a double-helix along the z axis of the microscope (Figure 3) [24]. The center of the DH-PSF gives the precise location of the fluorophores, while the orientation of the lobes when matched to a given calibration graph provides the location along the Z axis. The DH-PSF has been used successfully for super localization microscopy [6] and particle tracking [1, 25].

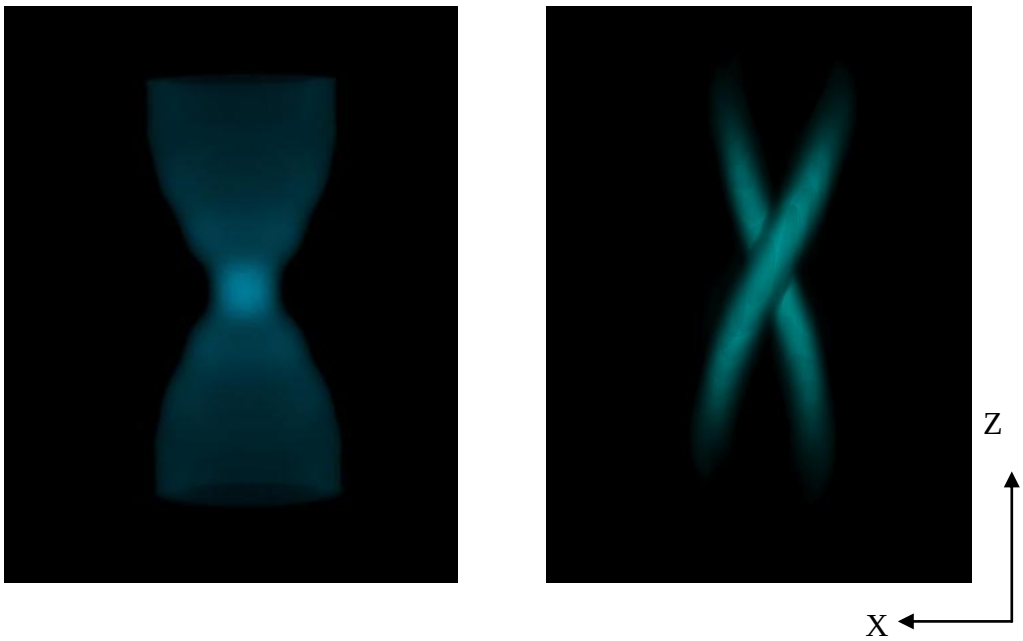

Figure 3. The 3D view of the Point Spread Function. **Left:** Conventional. **Right**:Double-Helix.

It is noted that the DH-PSF displays a significant change of orientation with defocus over an extended depth (Figure 3). In contrast, the standard PSF presents a slowly changing and expanding symmetrical pattern throughout the same region. Depth of focus (DOF) refers to the extent in the z direction where the point source remains in focus. In the conventional PSF, intensity change is at a minimum closer to the DOF while in the DH-PSF change is greatest at the DOF.

1.2.6. Computational Methods Matched to DH-PSF Engineering

The defocused DH-PSF can be used for determination of depth from rotation. A calibration curve can be generated for a system by plotting the angle of rotation of the DH-PSF's lobes versus distance along the imaging axis (Z) by moving a point source of light through known axial distances (Figure 4). Estimated rotation angles from any subsequent images acquired with a DH-PSF system are then compared to the calibration curve to yield the precise Z location of each imaged point source.

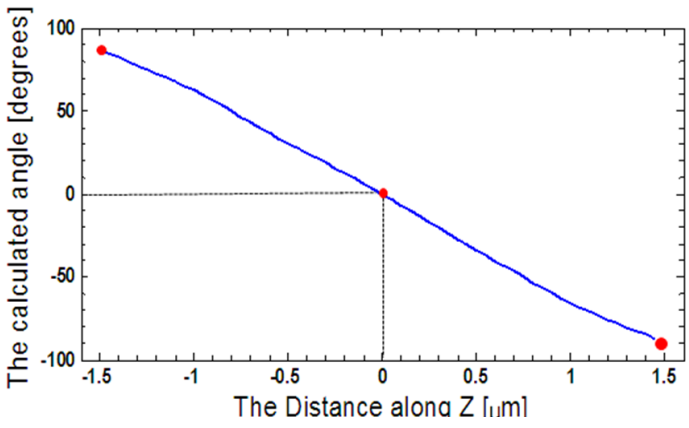

Figure 4. The calibration curve for 63X 1.4NA oil lens based system for a point source located at 1.5 μm above and below best focus.

As mentioned above, angle estimation is required for extracting depth information from the rotation of the DH-PSF. A simple angle estimation algorithm finds the highest intensity in the two lobes of the DH-PSF and interpolates them to create a line which subtends a certain angle with the horizontal axis. This angle is mapped back to a calibration curve to get the accurate Z position estimate.

Reconstruction algorithms for 3D de-blurring and pixel intensity estimation can also be used to process images from DH-PSF systems with knowledge of the DH-PSF(s) of the system. This is a new idea proposed and presented in this thesis.

1.3. Thesis Contribution

DH-PSF based systems being a nascent technology have not been thoroughly explored for all imaging conditions. In order to optimize the use of DH-PSF based systems testing under different aberrations is required so that appropriate steps can be taken to compensate for the aberrations. In this thesis, we study the effect of spherical aberrations on DH-PSF based systems since SA has an effect in the accurate localization of fluorophores (Figure 1). We also introduce the idea of using restoration algorithms to estimate the intensity in the underlying object. Processed images provide an accurate representation of the object. Since the DH-PSF system forms an intermediate image which is actually a distorted and blurred image, 3D image estimation is a vital step in making DH-PSF based systems more practical for precise 3D imaging.

As part of the thesis work, software to compute DH-PSFs with and without SA was developed and simulated images of a DH-PSF-based system were generated. Depth from

rotation using a previously developed angle estimation technique was investigated using these images and it was extended to apply to images with SA. In addition, the SIEM and DVEM algorithms of the COSMOS software package were applied to the simulated images and estimated results were compared to the true object in order to quantify performance. Finally, the frequency content and the performance of the DH-PSF based system were compared to those of the conventional microscope system.

2. Background Information on the Development and Use of DH-PSFs

2.1. DH-PSF Phase Mask Design

The genesis of a phase mask that generates the DH-PSFs came with the idea of wave propagation with rotating intensity distribution suggested by Piestun, Schechner, and Shamir [26]. Generalized self imaging (GSI) suggested by the same group [27], basically involves the superposition of Gauss Laguerre modes to display an effect of where the image does not change over the propagation length of a wavefront apart from rotation. A manifestation of the GSI system is the rotating beams, where the transverse intensity distribution is invariant upon propagation, except for continuous rotation. A spiral trajectory is described by the image pattern. The total rotation of from the best focus (waist) to the far field is a rational multiple of $\pi/2$.

Pavani, et al. [28] introduced a high efficiency rotating PSF. The transfer function efficiency was improved by optimizing the constraints in the spatial and frequency domain of the GL modal plane so as to obtain a 30% improved transfer function efficiency. Spatial light modulators (SLM) were modified to improve the efficiency.

Sharma et al. contributed to the optimization of the DH-PSF for 3D accuracy. The use of a phase only SLM with 80% greater efficiency than traditional phase masks to provide improved imaging using an iterative algorithm [29]. Quirin et al. extended the concept of DH-PSFs and combined it with extended depth of field imaging [4] to get axial ranging in a broad band 3D system.

2.2. Implementation of the DH-PSF in a Microscope System

A DH-PSF system can be implemented by introducing a phase mask in the Fourier plane of the imaging lens in a 4F system (Figure 5). The phase mask is designed such that its transmittance function generates a rotating pattern in the focal region of an ocular lens as discussed above.

A DH-PSF based microscope system with a reflective phase-only spatial light modulator (SLM) was presented in [1]. The system is composed of a sample located at the objective focal plane of a conventional inverted microscope and an optical signal-processing section. The signal-processing section is essentially a 4f imaging system.

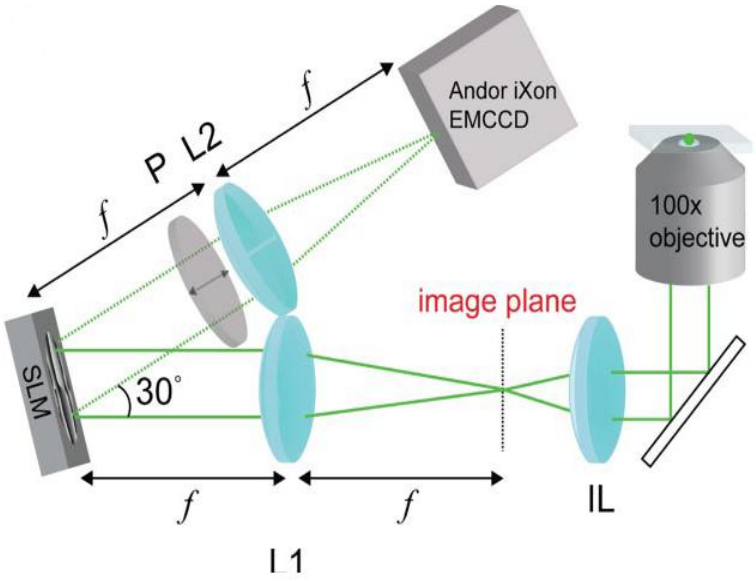

Figure 5. Collection path of the single-molecule DH-PSF setup. IL is the imaging (tube) lens of the microscope, L1 and L2 are focal-length-matched achromatic lenses, and SLM is a liquid crystal spatial light modulator. (Courtesy:[1])

Specifically, an achromatic lens L1 placed at a distance *f* from the microscope's image plane produces the Fourier transform of the image at a distance *f* behind the lens. The phase of the Fourier transform is modulated by reflection from the SLM. The final image

is produced by another achromatic lens L2 placed at a distance *f* after the SLM and recorded with an electron-multiplying CCD camera.

When the SLM is loaded with the DH-PSF phase-mask, the Fourier transform of the sample image is multiplied by the DH-PSF transfer function. Equivalently, every object point is convolved with 2 DH-PSF lobes, with the angular orientation of the lobes depending on the axial location of the object above or below focus.

2.3. The Use of DH-PSF in 3D Microscopy

Obtaining depth from defocus is a very popular and well explored technique [30] . At the DOF the PSF change is least for conventional PSF hence a circle of confusion is created where the depth cannot be determined accurately. DH-PSFs overcome this difficulty since rotation is greatest within the DOF. Greengard et al. [5] used the rotating beams to generate Rotating PSFs (another name for the DH-PSF) which could be used to extract the depth of a point source for microscopy based imaging. They demonstrated depth information was obtained with greater accuracy, using calibration curves with rotating PSFs.

Pavani, Piestun, et al. extended their study to 3D tracking of micro particles [1]. In this paper, the term double-helix PSF was coined, because rotating PSFs were stacked to give the double helical shape. The Fisher information content in DH-PSF was shown to be much higher than in conventional PSFs. Experiments demonstrated average position estimation accuracies under 14 nm and 37 nm in the transverse and axial dimensions respectively.

Pavani, DeLuca, and Piestun collaborated on an interdisciplinary study on studying single molecule imaging of cells with DH-PSFs [31] . Improved contrast was observed with PtK1 cells. Fluorescent protein embedded within cellular structure was super-localized. Information was obtained over two polarization sensitive channels to give an increment in efficiency. Another set of interdisciplinary studies done by Pavani et al. involved detection of polymer molecules in a polymer sample [6]. This paper emphasized on super localization of single molecules in a thick 3D sample. This concept was also explored in [24] . Badieirostami et al. [32]developed a method to improve imaging with DH-PSF based systems in presence of astigmatism and bi-plane aberrations.

Lew et al. [33] used DH-PSFs to image weak emitters in biological systems by tracking the movement of quantum dots in glycerol and in live cells series of proteins. Lord et al. [34] used dark push-pull chromophores which have the ability to produce bright fluorescent labels suitable for single molecule imaging. Thomson et al. used DH-PSFs to track single mRNA particles in *Saccharomyces cerevisiae* to improve understanding of biological particle behavior.

3. Forward and Inverse Imaging Problems

Mathematical modeling of the DH-PSF from the conventional PSF is first described and then a model of image formation in the presence of SA is reviewed and adapted for a DH-PSF based microscope system.

3.1. Mathematical Modeling of the DH-PSF

In optical sectioning microscopy when object points located deep in the specimen layer are imaged, light emitted by the observed object point must pass through layers whose thicknesses and refractive indices can vary significantly from the layers in the design system. This causes SA and results in degraded resolution and contrast in the 3D image [10]. SA is included along with defocus in the optical path length error, $W(u,v)$ in the imaging system's generalized pupil function [10]. The 2D intensity PSF, $h(x, y, z_i, z_o)$, defined as the image of a point source of light at depth $z = z_o$ in the specimen when the microscope is focused at a plane conjugate to the image plane at $z = z_i$ can be computed from the square magnitude of the Fourier transform of the generalized pupil function [35]. 2D PSFs stacked together in 3D they form a 3D PSF $h(x, y, z)$.

In a microscope system with a DH mask inserted at the back focal plane of the imaging lens, the phase of the generalized pupil function is further modified by the phase of the DH mask $\phi(f_x, f_y)$. By the definitions of the amplitude transfer function (ATF), i.e., that it is both a scaled version of the pupil function $H(f_x, f_y, Z_k) = P(\lambda z f_x, \lambda z f_y, Z_k)$

where (f_x, f_y) are scaled spatial frequencies in the back focal plane of the imaging lens and also it is defined as the Fourier transform of the complex-amplitude (or coherent) PSF, we can obtain the generalized pupil function by taking the Fourier transform of the coherent PSF (Figure 2b). The defocused ATF defined at each depth $z = Z_k$ and including SA is given by:

$$\begin{aligned} H(f_x, f_y, Z_k) &= F\{h_c(x, y, Z_k)\} \\ &= H(f_x, f_y) e^{j(2\pi/\lambda)W(f_x, f_y)} \end{aligned} \quad [2]$$

Where F{} is the Fourier transform operation, λ is the wavelength of light emitted by the point source, and $h_c(x, y, z)$ is the coherent PSF. Thus knowledge of the generalized pupil function (Eq. 3.1) allows the determination of a modified ATF for a system that includes a DH mask:

$$H_{DH}(f_x, f_y, Z_k) = H(f_x, f_y, Z_k) e^{j(2\pi/\lambda)\phi(f_x, f_y)} \quad [3]$$

The 2D DH-PSF at each depth $z = Z_k$ is computed by taking the square magnitude of the Fourier Transform of the modified ATF. The 2D DH-PSFs are stacked along Z to obtain the 3D DH-PSF:

$$h_{DH}(x, y, Z_k) = \left| \mathrm{F}^{-1} \; H_{DH}(f_x, f_y, Z_k) \right|^2 \quad [4]$$

3.2. Image Formation with a DH-PSF Based System

In the absence of SA image formation with DH-PSFs is mathematically modeled by the convolution of the intensity DH-PSF with the object.

$$g_{DH}(\mathbf{x}_i) = \iiint_0 h_{DH}(\mathbf{x}_i - \mathbf{x}_o) s(\mathbf{x}_o) d\mathbf{x}_o \quad [5]$$

where $\mathbf{x_i} = (x_i, y_i, z_i)$ which represents a 3D point in the image plane and $\mathbf{x_o} = (x_o, y_o, z_o)$ 3D point in object space O. $h_{DH}(\mathbf{x}_i - \mathbf{x}_o)$ is the PSF and $s(\mathbf{x}_o)$ is the specimen function. $g_{DH}(\mathbf{x}_i)$ is the intensity of the image for a DH-PSF based system.

3.3. Image Formation with DH-PSF based system in the Presence of SA

Image formation in a depth variant imaging system can be written as [16]

$$g_{DH}(\mathbf{x}_i) = \iiint_O h_{DH}(x_i - x_o, y_i - y_0, z_i, z_o) s(\mathbf{x}_o) d\mathbf{x}_0 \quad [6]$$

where $\mathbf{x}_i = (x_i, y_i, z_i)$ which represents a 3D point and $\mathbf{x}_0 = (x_o, y_o, z_o)$ a 3D point in object space O. $h(x_i - x_o, y_i - y_o, z_i, z_o)$ is the depth varying PSF and $s(\mathbf{x}_0)$ is the specimen function. $g_{DH}(\mathbf{x}_i)$ is the intensity of the image for a DH-PSF based system with SA.

3.4. Solving the Inverse Imaging problem Using the Strata Approximation Model

The depth-variant strata model [16] can be used to approximate Eq. [6] and hence the DVEM algorithm presented in [16] can be used to solve the inverse imaging problem. The strata model and the DVEM algorithm are briefly reviewed here for completeness.

For restoration purposes the object plane is divided into M non-overlapping strata thus the object can be rewritten as $s(\mathbf{x}_o) = \sum_{m=1}^{M} s_m(\mathbf{x}_o)$. PSFs are calculated at depths $z_i = Z_m$ where m=1, 2, 3….. M. The PSF associated with $s_m(\mathbf{x}_i)$ is the interpolation of the PSFs at depths of $z_i = Z_m$ and $z_i = Z_{m+1}$

$$\tilde{h}_m(\mathbf{x}_i, \mathbf{x}_o) = a_m(z_o) h_m(\mathbf{x}_i - \mathbf{x}_o) + [1 - a_m(z_o)] h_{m+1}(\mathbf{x}_i - \mathbf{x}_o) \quad [7]$$

where $a_m(z_o) = \begin{cases} \dfrac{Z_{m+1} - z_o}{Z_{m+1} - Z_m} \\ 0 \end{cases}$

Thus the approximate image intensity at each stratum

$$g_m(\mathbf{x}_i) = \iiint_O \tilde{h}_m(\mathbf{x}_o, \mathbf{x}_i) s_m(\mathbf{x}_o) d\mathbf{x}_o \quad [8]$$

Thus the image intensity can be written as

$$g(\mathbf{x}_i) \approx \sum_{m=1}^{M} g_m(\mathbf{x}_i) \quad [9]$$

EM-ML restoration was implemented on this model in [16] where the DVEM algorithm was presented. In this thesis we use the DVEM algorithm with the DHPSF. At the end of every iteration the estimation step can be written as

$$\hat{s}^{(k+1)}(\mathbf{x}_o) = \frac{\hat{s}^{(k)}(\mathbf{x}_0)}{H_M}\ a_m(z_o) d_m^{(k)}(\mathbf{x}_o) + [1 - a_m(z_o)] d_{m+1}^{(k)}(\mathbf{x}_o) \qquad [10]$$

k is the iteration number and $\hat{s}(\mathbf{x}_0)$ is the estimation of the object

where $d_m^{(k)}(\mathbf{x}_o) = \int_I h_m(\mathbf{x}_i - \mathbf{x}_o) r^{(k)}(\mathbf{x}_i) d\mathbf{x}_i$

and $r^{(k)}(\mathbf{x}_i) = g(\mathbf{x}_i) / g^{(k)}(\mathbf{x}_i)$, ratio of the image and the estimated image at the kth iteration while $h_m(\mathbf{x}_i - \mathbf{x}_o)$ is the DH-PSF at the mth depth.

$$H_m(z_o) = \sum_m \{a_m(z_o) H_m + [1 - a_m(z_o)] H_{m+1}\},$$
$$H_m = \int_I h_m(\mathbf{x}_i - \mathbf{x}_o) d\mathbf{x}_i$$

The algorithm starts with an initial guess and converges to the object. Changing the number of strata gives us a more accurate representation of real system since in microscopy the PSF changes with depth but computational time increases linearly with the number of strata (or PSFs) used for the data processing. Thus a trade-off exists between computational complexity and accuracy of the estimated result.

Using the modeling described above simulations are generated to study the DH-PSF based system. DH-PSF systems are described both in the spatial and frequency domain. In the next section we look at frequency domain properties of the DH-PSF system.

4. The DH-PSF and its Frequency Content

In this chapter we shall discuss in depth the DH-PSF based systems. We will go over the implementation procedure, frequency analysis and also observe the contrast and similarity with conventional-PSFs.

4.1. Computation of the DH-PSF

In order to investigate the effects of SA on DH-PSF as well the ability of estimation algorithms to recover underlying objects from images of a system characterized by a DH-PSF, PSFs were computed for different imaging conditions using the COSM open source (COSMOS) software package [14] and a Matlab script(included in the Appendix of this thesis). The COSMOS PSF module allows the user to compute PSFs for different lenses and imaging conditions viz. wavelength, RI of the immersion medium and specimen, NA of the lens, etc. that cause SA. Users have a choice of using either the models developed by Gibson and Lanni [10] or Haeberle [36] to generate the PSFs. The latest version of COSMOS (COSMOS 8.0.9 and higher) offers the functionality which provides the real and imaginary part of the coherent PSF in addition to the incoherent (intensity) PSF. This functionality was added to facilitate the computation of the DH-PSFs.

The Gibson and Lanni model in the COSM PSF module of COSMOS 8.0.9 was used to create complex-valued conventional depth-variant coherent PSFs for a 63X 1.4 N.A oil lens, defined for point sources at different depths within a watery specimen (RI = 1.3) for

emission wavelength equal to 633 nm and pixel size of 50 nm in all directions. For all the simulations described here the same imaging conditions were used.

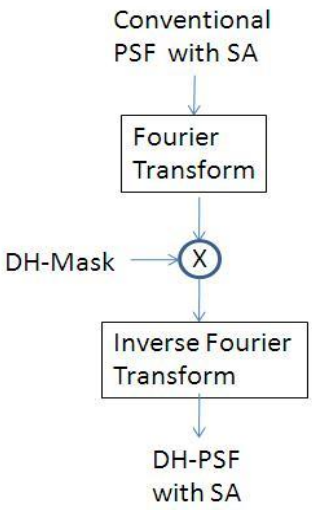

Figure 6. Schematic diagram for the computation of the DH-PSF starting from the conventional complex-amplitude PSF by incorporating the DH-Mask to the generalized pupil function.

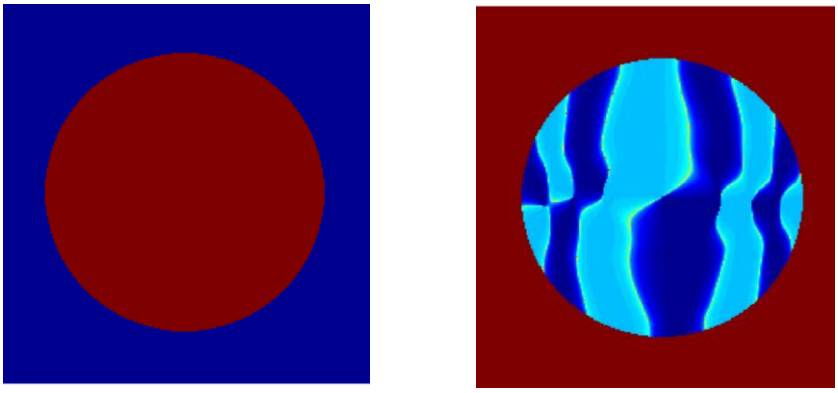

Figure 7. The amplitude of the DH-mask (a), the phase of the DH-mask (b).

The block diagram in (Figure 6) was implemented using a Matlab script. As shown in the figure, the 2D inverse Fourier transform of each XY plane of PSFs (the real and imaginary parts generated from COSMOS) was computed to produce a generalized pupil

function (Eq.2). The DH phase mask (Figure 7) was multiplied to generate the generalized double helix pupil function (Eq. 3) .The Fourier transform of the double helix pupil function was computed to obtain a 2D DH-PSF with spherical aberration (Eq. 4). The square of it was taken to get the DH-PSF intensity. The process was repeated for all the planes in the 3D PSF resulting in a 3D PSF.

The mask design used in this thesis was obtained from our collaborator Dr. Piestun at the Univ. of Colorado, Boulder in the form of numerical data on a 256x256 pixels grid for a pupil of size 185x185. The pupil size needed to be matched to this mask, since if the pupil is smaller or larger than 185 pixels then the singularities fail to affect the light passing through it. During this study the mask was resampled using the *imresize* function pre-defined in matlab so that the number of pixels in the mask map to the number of pixels used to discretize the diameter of the imaging pupil. The pupil diameter (*D*) is twice the cutoff frequency, $f_{cutoff} = N.A./\lambda$ of the coherent imaging. The pixel size in the frequency domain along the f_x axis is $df_x = 1/(N \times dx)$, where dx is the pixel size along the *x*-axis in the space domain. Thus the pupil diameter in pixels is given by

$$\#\text{ of pixels along } D = 2 f_{cutoff} / df_x = 2(f_{cutoff} \times N \times dx) \qquad [11]$$

N is the total number of pixels along the *x*-axis for the image grid used, and λ is the wavelength of the light imaged by the system. The pupil diameter changes with the N.A. of the lens, therefore computation of DH-PSFs for different lenses requires mapping the size of the mask accordingly.

The N.A. together with the wavelength affect the degree of rotation of the DH-PSF. Using a lower N.A. DH-PSF based system (i.e., N.A. = 0.45 air lens) a longer

distance along Z (~10 μm in Figure 2) can be covered without losing the property of obtaining depth from rotation On the other hand, for a higher N.A. system the distance along Z is much lower (e.g. for N.A. = 1.4 the distance is 3.2 μm as shown in Figure 8). This is due to the ability of the DH-PSF to rotate for a limited range along the Z axis mapping to rotation angles from -90 to 90 degrees. The range of rotation is dependent on ($\sim \frac{\lambda}{N.A.}$) where λ is the wavelength and *N.A.* is the numerical aperture of the lens.

4.2. Comparison between DH and Conventional PSFs

The CosmPSF module was used to generate 5 depth-variant PSFs (Fig. 7) with increasing spherical aberration for a system with a 63X 1.4 N.A oil lens, defined for point sources at different depths within a watery specimen (RI = 1.3) for emission wavelength equal to 633 nm and pixel size of 50 nm. Figure 10 shows the DH-PSFs and Conventional PSFs with increasing SA.

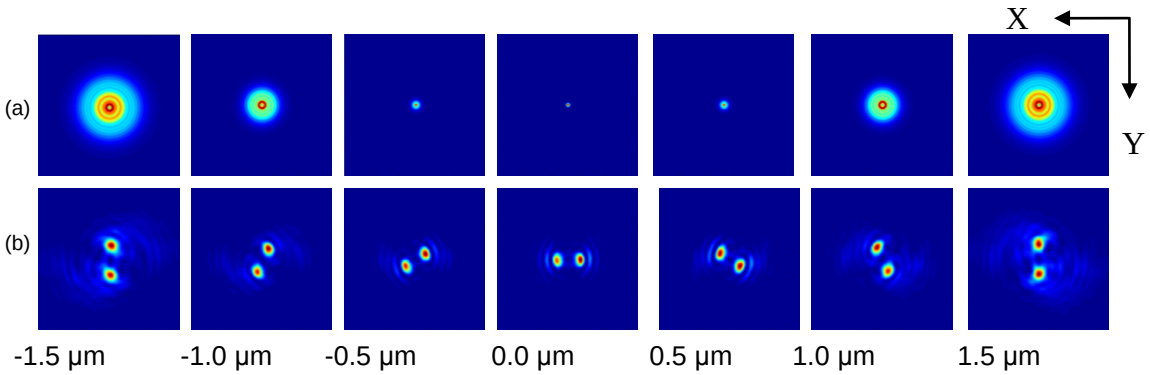

Figure 8. Comparison of 2D defocused PSFs for a 63x/1.4 N.A oil lens with 633 nm wavelength computed at different imaging depths (depth of focus) from -1.5 μm to 1.5 μm with best focus at 0 μm. (a) Conventional 2D PSF; (b) 2 D DH-PSF.

The XY view through defocus for conventional PSF and DH-PSF (Figure 8) and a system with SA (Figure 9) shows the rotation of the DH-PSF and the blurring of the point source. The geometry of the DH-PSF is very different from conventional PSF. The point source appears as a two lobed structure for DH-PSF system. Over the range of defocus (3.0 μm) the DH-PSF shows more easily realizable variation than the conventional PSF and hence can be used for super localization. Thus the depth from rotation (using DH-PSF) is easier realized than depth from defocus (using conventional PSF). For high N.A. systems the rate of rotation is faster hence the defocus distance covered is much shorter.

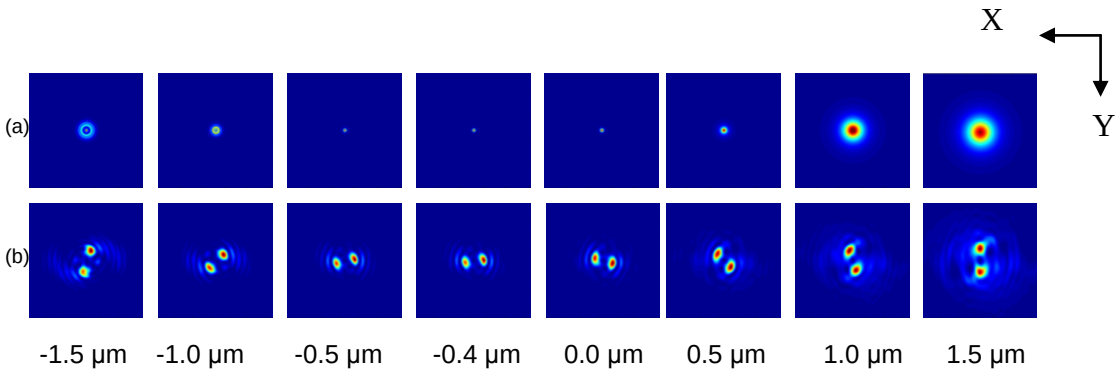

Figure 9. Comparison of 2D defocused PSFs for a 63x/1.4 N.A oil lens with 633 nm wavelength computed at different imaging depths (depth of focus) from -1.5 μm to 1.5 μm with SA at 2.4 μm and best focus at -0.4 μm. (a) Conventional 2D PSF; (b) 2D DH-PSF.

The 2D PSFs at each Z location are stacked on top of each other extending from over 256 planes for our experiments i.e. from -12.5 μm- 12.5 μm. This gives us a 3D volume, which is the 3D PSF of the system. The XZ views of this 3D system are observed in Figure 10. Due to the effect of SA point sources lying at different depths within the sample have different 3D PSFs. In the subsequent figure we will look at 3D

PSFs generated from point sources lying at different depths within a watery sample with R.I. 1.33 viz. 0 μm, 0.9 μm, 1.8 μm, 2.7 μm and 3.6 μm.

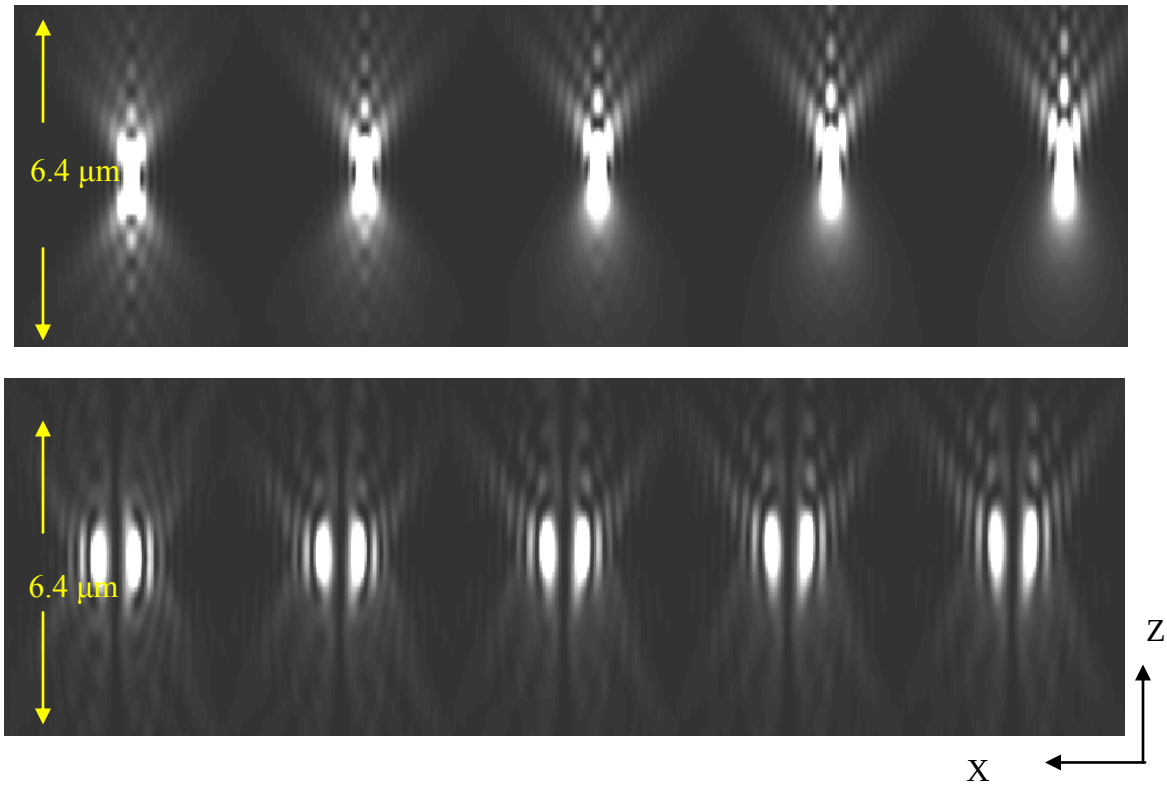

Figure 10. Top Row: XZ cut-view images of the conventional intensity PSFs for a 63X 1.4 N.A oil lens (RI = 1.512) computed for point sources of light at depths 0 μm, 0.9 μm, 1.8 μm, 2.7 μm and 3.6 μm (from left to right) in a watery medium (RI = 1.33). Bottom Row: The XZ cut-view images of the DH-PSFs corresponding to the same point sources of light as in the case of the conventional PSFs in the top row.

For the SA based system there is a shift in the best focus of the system for conventional PSFs along with an asymmetry of lobes along Z. The DH-PSF is supposed to be valid over a small defocus. For DH-PSFs the asymmetry along Z is not so pronounced but there is a shift in the best focus of the system i.e. the point where the lobes of the DH-PSF is horizontal to the axis. This shift is the same (0.4 μm) between the conventional and DH-PSF with SA at 2.4 μm depth.

4.3. Frequency Content of the DH-PSF

Depth-induced SA due to a refractive-index (RI) mismatch between the immersion medium and the RI of biological samples are known to worsen when imaging deep inside the specimen and change the PSF of the microscope at each imaging depth rendering the system depth variant as seen in (Figure 10). In this section we investigate the frequency content for the DH-PSF of a wide-field fluorescence microscope in the presence of depth-induced SA by computing the DH optical transfer function (OTF). 2D defocused DH-OTFs were computed as well as the 3D DH-OTF. The DH-OTFs were compared to the OTFs of the conventional wide-field fluorescence microscope.

The 3D OTF is the frequency domain representation of the incoherent 3D PSF i.e. it is Fourier transform of the intensity PSF [35] Conventional OTFs are shaped like a torroidal donut with a missing cone of frequencies in the center which account for loss of resolution. Many methods with the COSI approach try to fill in this missing cone of frequencies by manipulation of the PSF. The frequency content of the DH-PSFs has not been studied in detail prior to this study.

The normalized magnitude of the OTF known as the MTF of the system is computed from the DH-PSF using Eq. (12):

$$MTF_{dh}(f_x, f_y, f_z) = \frac{|\mathrm{F}(h_{dh}(x,y,z))|}{\max(|\mathrm{F}(h_{dh}(x,y,z))|)} \quad [12]$$

The Phase transfer function (PTF) is also obtained from the DH-PSF using Eq. (13):

$$PTF_{dh}(f_x, f_y, f_z) = phase(\mathrm{F}(h_{dh}(x,y,z))) \quad [13]$$

$$OTF_{DH} = MTF_{DH} \times PTF_{DH} \quad [14]$$

The defocused 2D MTFs of the system without SA is shown in Figure 11. The plots of the cross section through the centre of the conventional MTF along x-axis (Figure 12) and DH-MTF along X axis (Figure 13) and Y axis (Figure 14) are shown below.

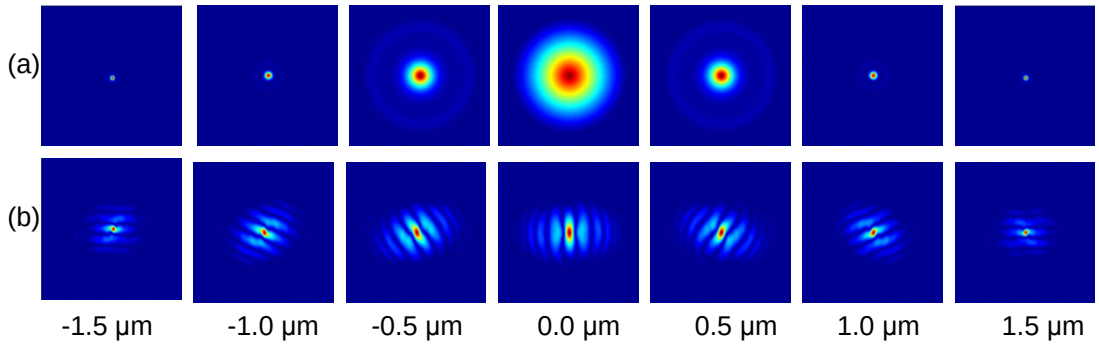

Figure 11. Comparison of 2D MTFs computed from the Fourier transform of the PSFs (Figure 9). (a) Conventional PSF system; (b) DH-PSF system.

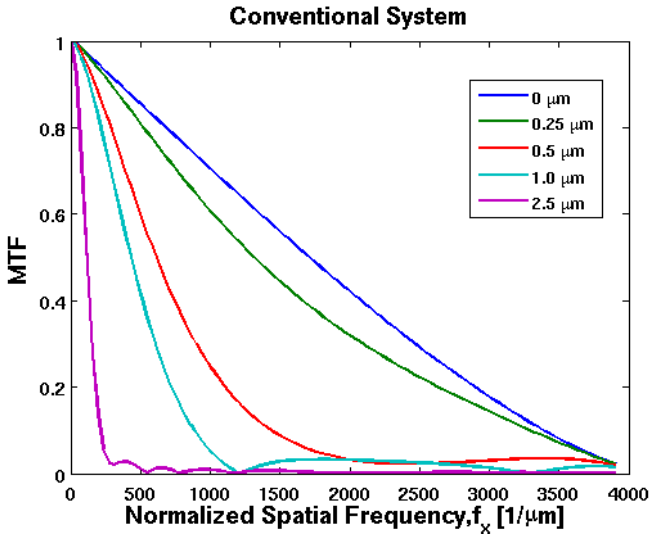

Figure 12. Profile along f_x through the Conventional 2D MTF with no SA (Figure 11).

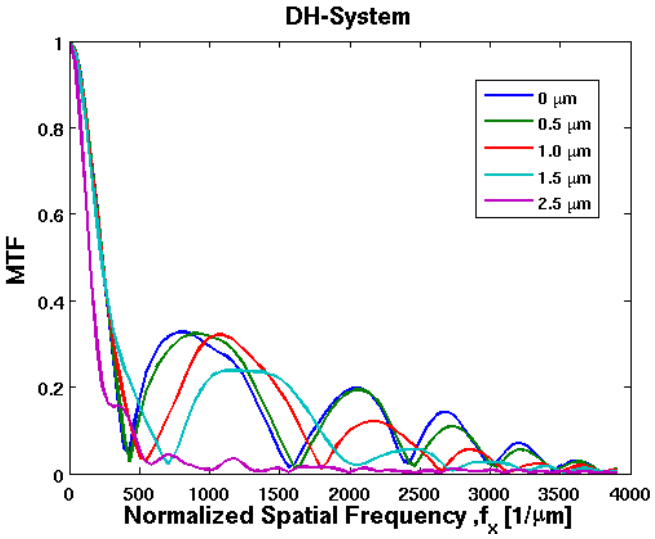

Figure 13. Profile along f_x through the DH 2D MTF with no SA (Figure 11).

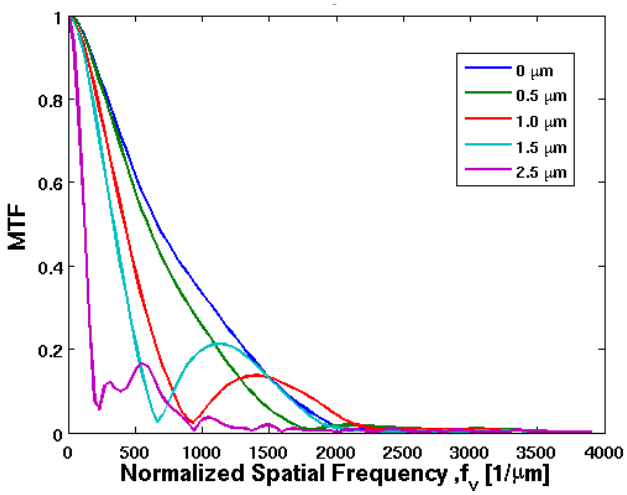

Figure 14. Profile along f_y through the DH 2D MTF with no SPA (Figure 11).

There is a redistribution of frequencies in the DH-MTFs when compared to the conventional system. The rotation is preserved in the DH-MTFs akin to Figure 8.There is a change between the plots of DH-MTF along f_x (Figure 13) and f_y (Figure 14) due to the asymmetry between X and Y axes which is not present for conventional MTFs. Over the range of rotation there is good preservation of the magnitude of the DH-MTFs

frequencies despite having more low frequencies than conventional MTF (Figure 12, Figure 13 and Figure 14).

The frequency analysis of SA images from both the DH-PSF based systems and conventional systems at 2.4 μm is studied to observe the effect of SA. The 2D MTF corresponding to the SA PSFs (Figure 9) are shown in Figure 15. The plots of the cross section through the centre of the conventional MTF along X axis (Figure 16) and DH-MTF along X axis (Figure 17) and Y axis (Figure 18) are shown below.

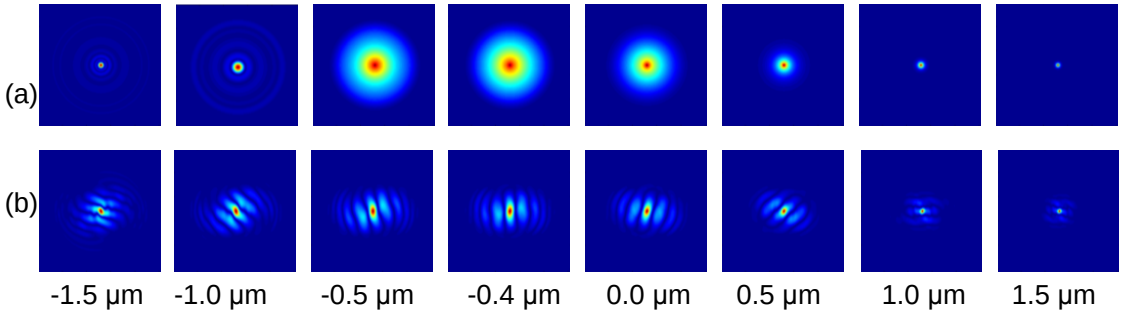

Figure 15. Comparison of 2D MTFs computed from the Fourier transform of the PSFs shown in (Figure 9): (a) Conventional PSF system; (b) DH-PSF system.

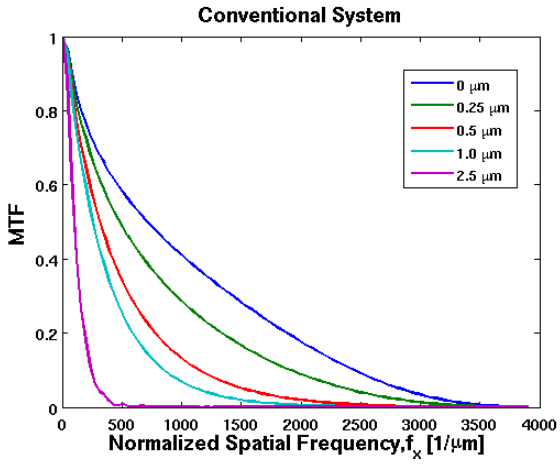

Figure 16. Profile along f_x through the Conventional 2D MTFs with SA (Figure 15).

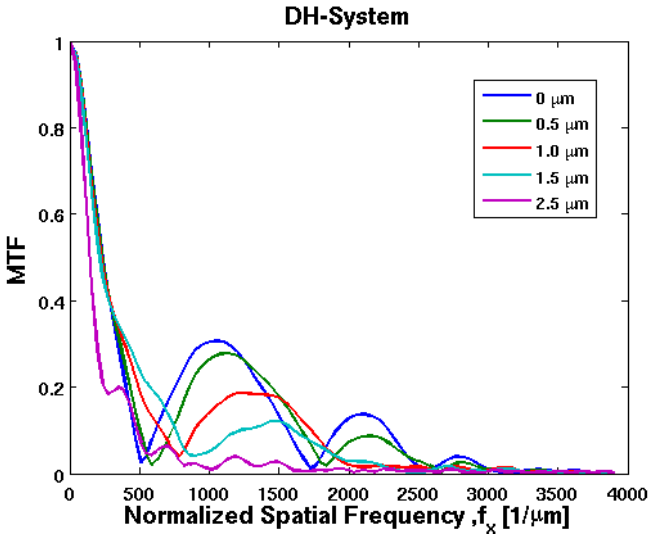

Figure 17. Profile along f_x through the DH 2D MTF with SA (Figure 16).

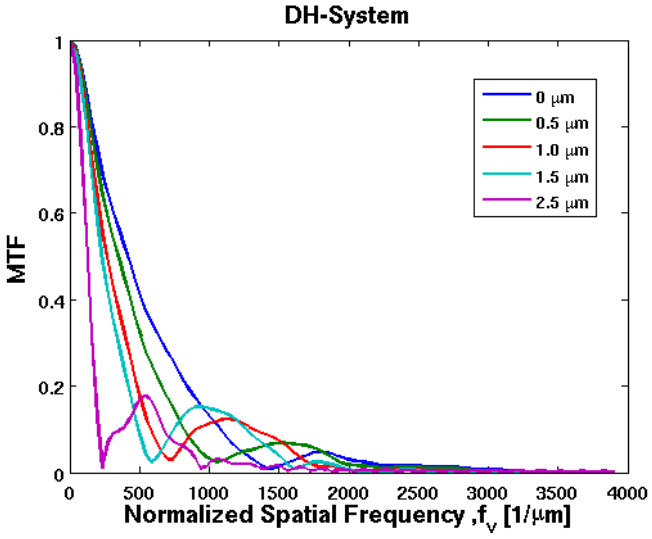

Figure 18. Profile along f_y through the DH 2D MTF with SA (Figure 16).

DH-MTF has extended depth of field that preserves spatial frequencies with defocus or SA compared to the MTF for a conventional system (Figure 15). The observed rotation in the 2D defocused DH-MTFs encodes depth information. There are redistribution frequencies in the 2D DH-MTF which contribute to the rotation and lobes

of the fluorophores (Figure 15). With SA there is a shift in frequency profile of the 2D MTF for both the DH-MTF and the conventional MTF which is similar to the PSFs. Over the range of rotation there is less attenuation in DH-MTFs than in conventional MTFs (Figure 16). There is also an attenuation of frequencies with SA for DH-MTFs (Figure 16 and Figure 12).

The 3D OTF was obtained from the PSFs for both the systems. The conventional OTF (Figure 19) traditionally has a missing cone of frequencies which contribute to the loss of resolution.

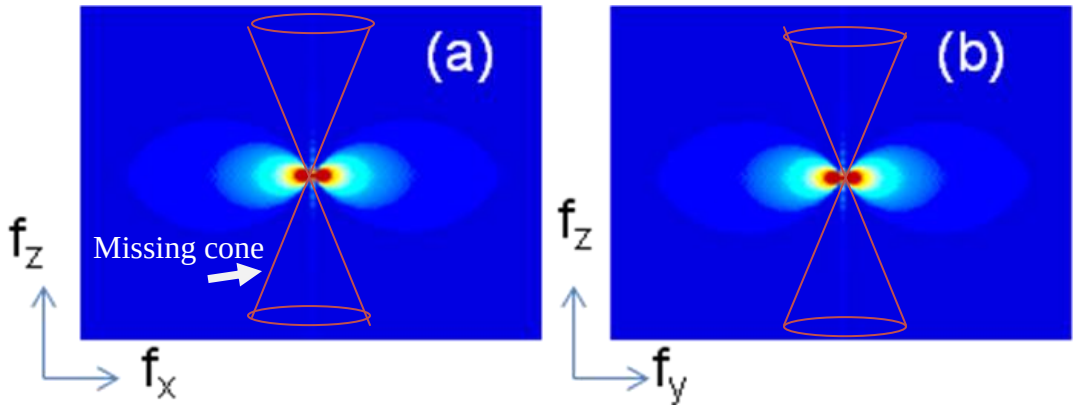

Figure 19. The 3D MTF along (a) $f_x f_z$ and (b) $f_y f_z$ for a conventional system with

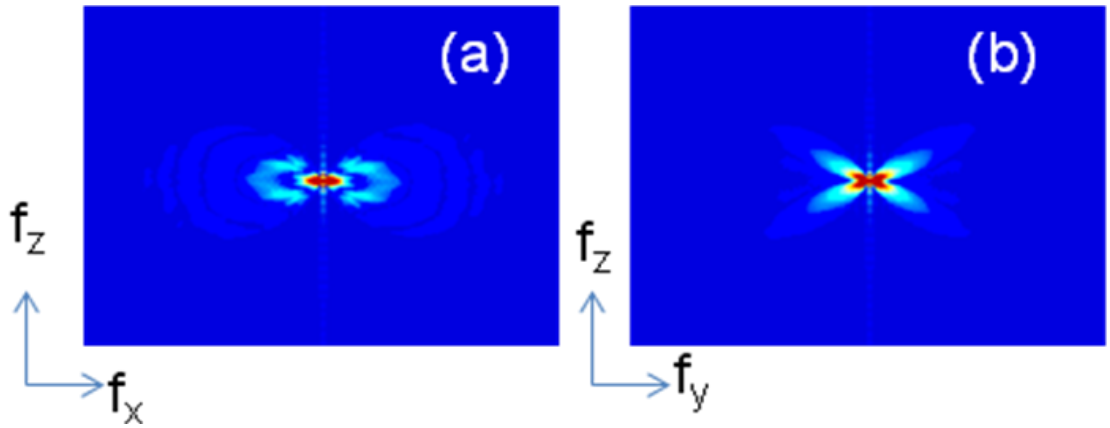

Figure 20. The 3D MTF along (a) $f_x f_z$ and (b) $f_y f_z$ for a DH-PSF based system with no SA.

The missing cone of frequencies in conventional PSF is preserved in the DH-PSF (Figure 20). The conventional system shows symmetry over f_x and f_y contrary to the DH-MTF. The DH-MTF along f_y shows a considerable loss of the frequency support. There are more low frequencies through the DH-MTF than the conventional MTFs (Figure 20). The PTFs of the systems were studied in Figure 21.

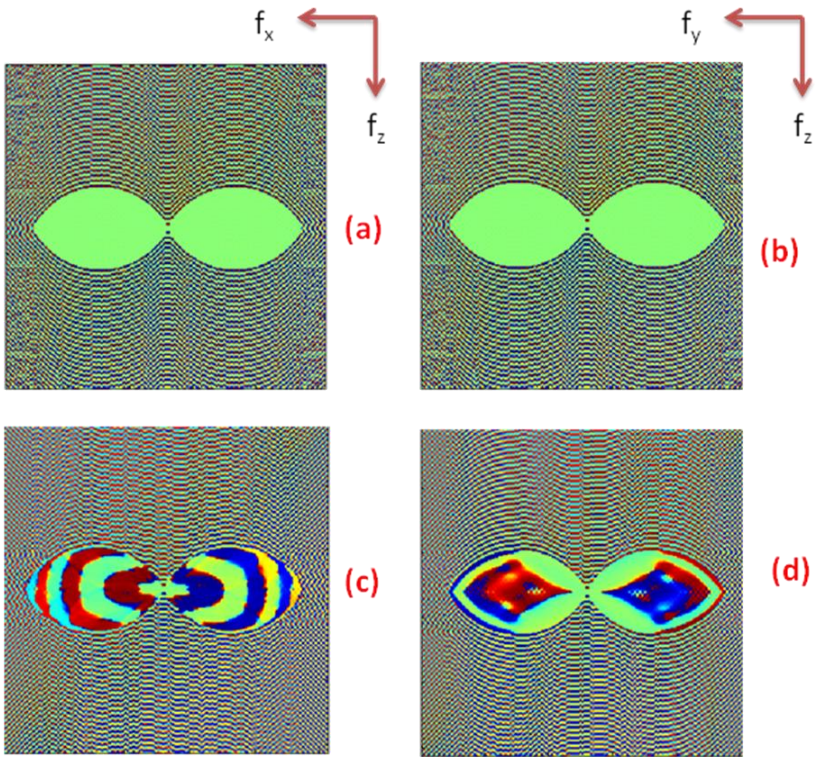

Figure 21. The PTF of Conventional and DH-PSF based system without SA. Conventional PTF with no SA along $f_x f_z$ (a), Conventional PTF with no SA along $f_y f_z$ (b), DH-PTF with no SA along $f_x f_z$ (c) and DH-PTF with no SA along $f_x f_z$ (d).

The 3D PTFs shown in Figure 21 show that the DH- system has higher phase content than conventional systems. The conventional phase is zero while the DH-PTF phase can be attributed to the mask.

The 3D OTFs are calculated for SA conventional system (Figure 22) and DH-PSF based system (Figure 23).

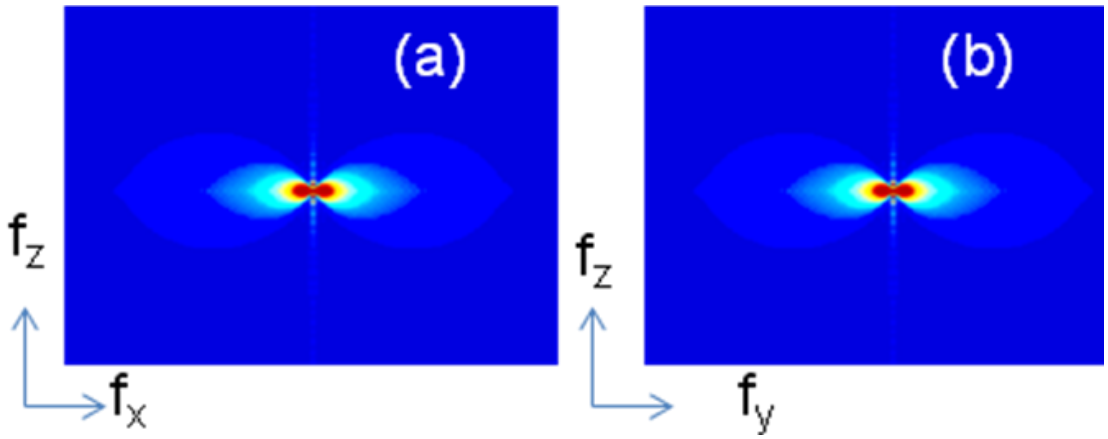

Figure 22. The 3D OTF along (a) $f_x f_z$ and (b) $f_y f_z$ for a Conventional system with SA.

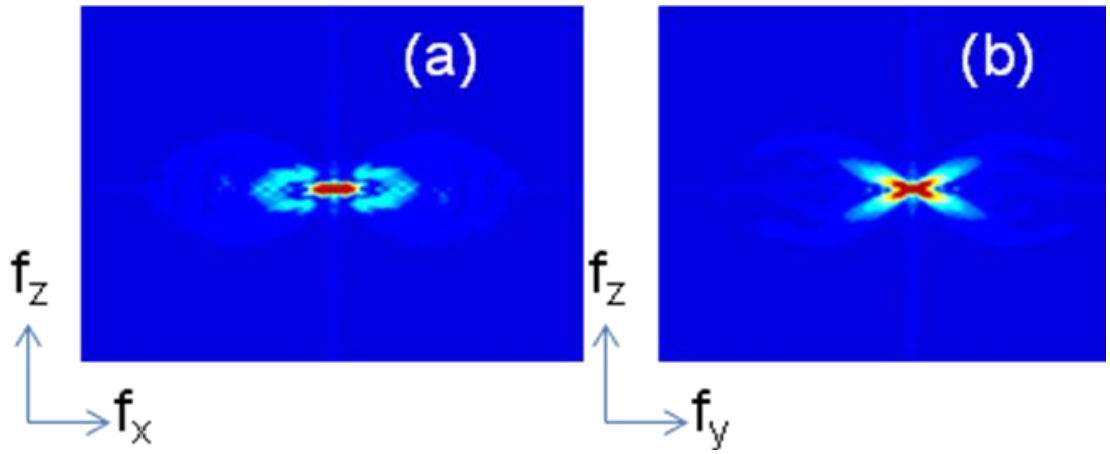

Figure 23. The 3D OTF along (a) $f_x f_z$ and (b) $f_y f_z$ for a DH-PSF based system with SA.

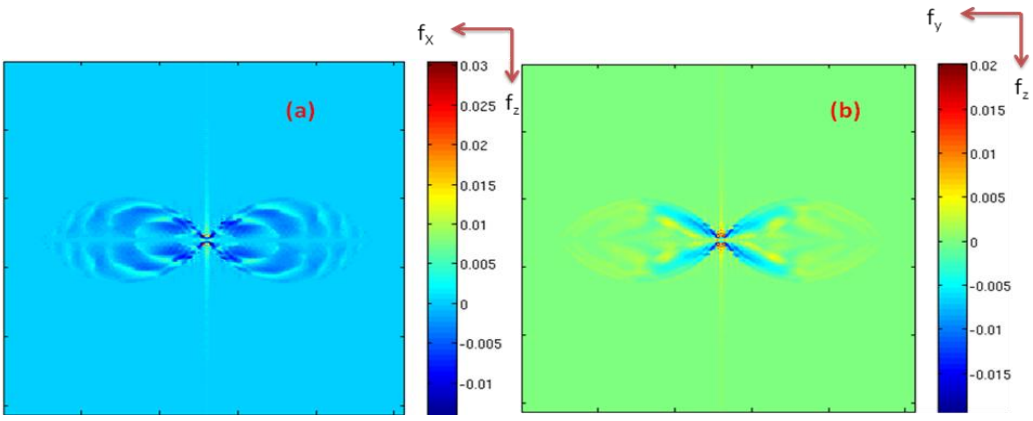

Figure 24. The value of the difference image computed by subtracting the 3D DH-MTF without SA from the one with SA along (a) $f_x f_z$ and (b) $f_y f_z$.

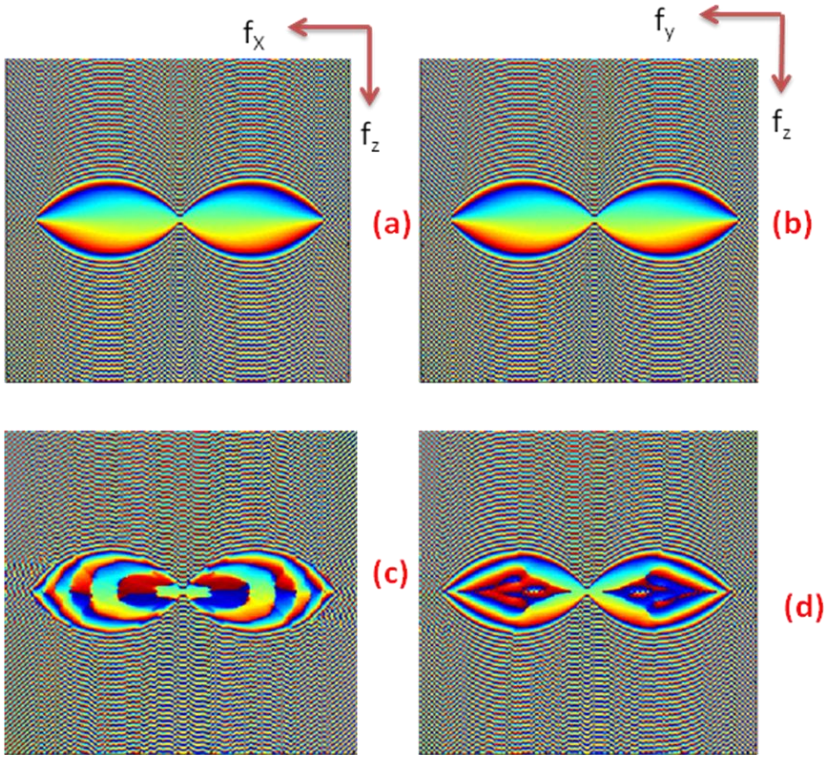

Figure 25. The PTF of Conventional and DH-PSF based system with SA. Conventional PTF with no SA along $f_x f_z$ (a), Conventional PTF with no SA along $f_y f_z$ (b), DH-PTF with no SA along $f_x f_z$ (c) and DH-PTF with no SA along $f_x f_z$ (d).

The 3D PTFs (Figure 21) show that the DH- system has greater variations in the phase content than conventional systems. In conventional systems the phase content is symmetric while in the DH-PTFs there is marked asymmetry.

The $f_x f_z$ and $f_y f_z$ views of the conventional OTF are identical while for a DH system the difference is marked because the DH-PSF is not circularly symmetric. There are additional missing frequencies for DH systems. There is an observed increase in the frequency support of the spherically-aberrant 3D DH-MTF (Figure 22), compared to the DH-MTF without SA. The missing cone is preserved in the DH systems consistent with conventional systems.

5. Depth Estimation from DH-PSF Rotation

One of the greatest advantages of DH-PSF based system is that a single 2D image at any plane can give us depth information about structures located throughout the whole 3D volume. This results in reduction of required images which not only reduces the image acquisition time but also reduces photo-bleaching effects. Depth of different point sources lying throughout the medium can be obtained by mapping the rotation angle of the identified DH-PSF like lobes to a standard calibration curve (Figure 4). In this section we will explore the effect of SA on super localization of point sources and calibration curves required in this process.

5.1. DH-PSF Calibration Curves DH-PSF

As mentioned earlier, a calibration curve (Figure 4) maps the angle of rotation of the DH-PSF lobes to the corresponding Z location. Such a curve can be generated from a DH-PSF by computing the rotation angle for each Z plane in the 3D DH-PSF (Figure 8).

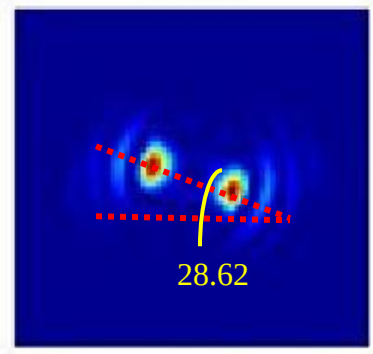

Figure 26 . Obtaining the angle subtended by DH-PSFs by interpolating between the locations of the two pixels with the highest intensity within the two lobes.

The angle subtended by a line between the two lobes of the DH-PSF and the horizontal axes in an XY plane is calculated using an algorithm developed at Dr. Piestun's laboratory at the University of Colorado, Boulder, which first computes the location of the highest intensity point within each lobe and then interpolates a line between the two locations (Figure 26). The angle subtended by this straight line with the horizontal axes provides the angle of rotation of the DH-PSF.

5.2. Calibration Curves for Spherically Aberrant DH-PSFs

The calibration curve for DH-PSFs for point sources located at depths of 0 μm, 0.8μm, 1.6 μm, 2.4 μm and 3.2 μm within the watery sample, were calculated for a RI mismatched system in other words a system with SA.

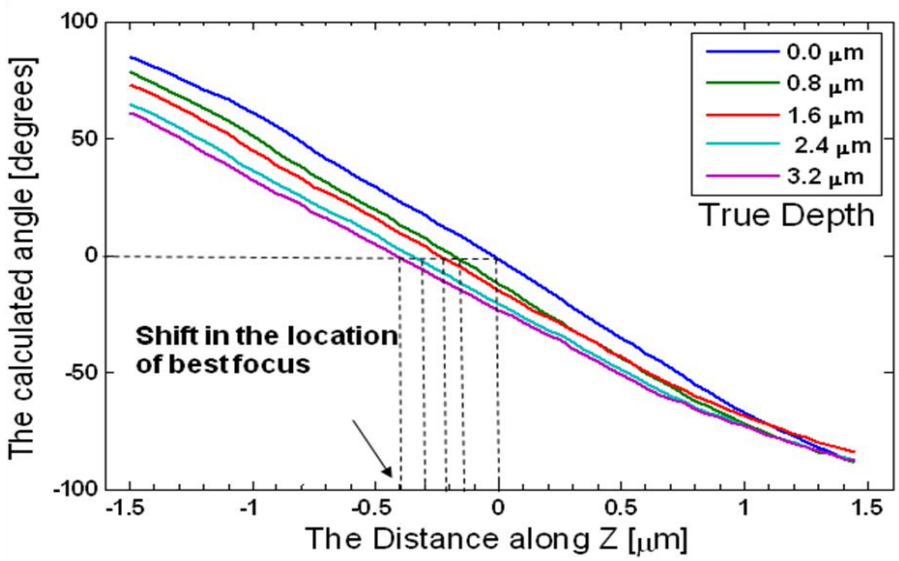

Figure 27. Calibration curves for a 63X 1.4NA oil lens (R.I.=1.517) DH-PSF based system from -1.5 μm to 1.5 μm computed from DH-PSFs due to a light point source located at depths of 0 μm, 0.8μm, 1.6 μm, 2.4 μm and 3.2 μm in a medium with RI = 1.33.

With increment in SA there is an axial shift in the best focus of the PSF (Figure 23) i.e. the point where the lobes of the DH-PSF are parallel to the horizontal axis. This is a phenomenon observed due to the SA (Figure 1). The slope of the curve decreases with increase in SA which means that the rotation of the lobes is slower hence loss of resolution along Z occurs (Figure 27).

5.3. Second Calibration Curve

In order to overcome the loss of axial localization precision due to the SA effect, we introduce a second calibration curve (Figure 28) which maps the axial shift to the depth of the point source i.e. it maps the true depth to the apparent depth shown also in Figure 1.

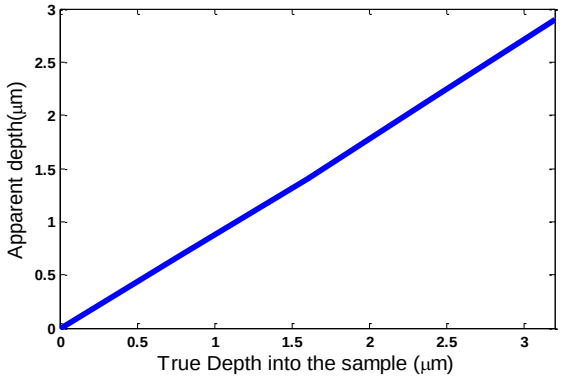

Figure 28. Second calibration curve with true depth mapped to apparent depth when a 63X 1.4 N.A oil lens is used to image a watery sample.

5.4. Simulated Images for Axial Localization

For the experiments presented here, two different objects were simulated to give rise to specific imaging conditions in which information about depth of point sources could be beneficial. A 3-bead object was simulated on a 256x256x256 window to demonstrate axial localization using calibration curves and further correction for SA using a second calibration curve. In addition, an elongated object was also used to demonstrate the effect of DH-PSF on elongated object and the length of the object was determined empirically using 2 point source markers.

5.4.1. Three Bead Object

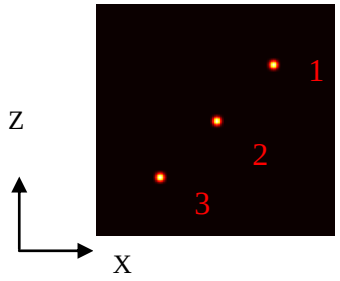

Figure 29. The 3 bead object in a 64x64 XZ view.

The three bead object comprises of three small spheres 50 nm in diameter located within a watery sample (RI=1.33) at depths of 0 μm, 1.5 μm and 3.0 μm. The object window is taken to be 256x256x256 pixels so that windowing effect can be prevented. Simulated images of this object were generated using for both a DH–PSF based system and a conventional system using PSFs with and without SA.

5.4.1.1. Images without SA

Equation (5) is implemented in the COSMOS Tools module which was used to compute the images shown in (Figure 30 and Figure 31).

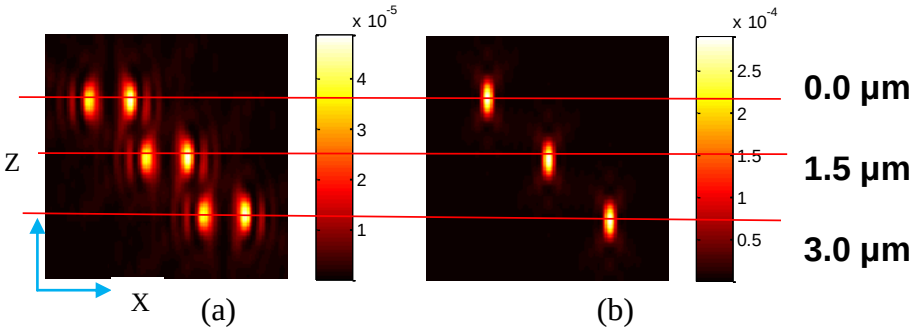

Figure 30 . Image with DH-PSF (a) and conventional PSF (b) with no SA with the 3 bead object.

During 3D imaging plane by plane acquisition of images take place which are stacked to get the 3D volume. In conventional system the user needs to scan through the planes to reach every plane where the object is sharpest and again start over again to obtain the next object. For a 3 bead object at least 60 planes need to be scanned to obtain the location of each object and also the image. In the DH-PSF based images a single plane suffices to provide information about the entire volume provided it's within the range of rotation of the DH-PSF (Figure 31). This is a major advantage of DH-PSF based systems and helps to reduce the number of images required hence reduces photobleaching.

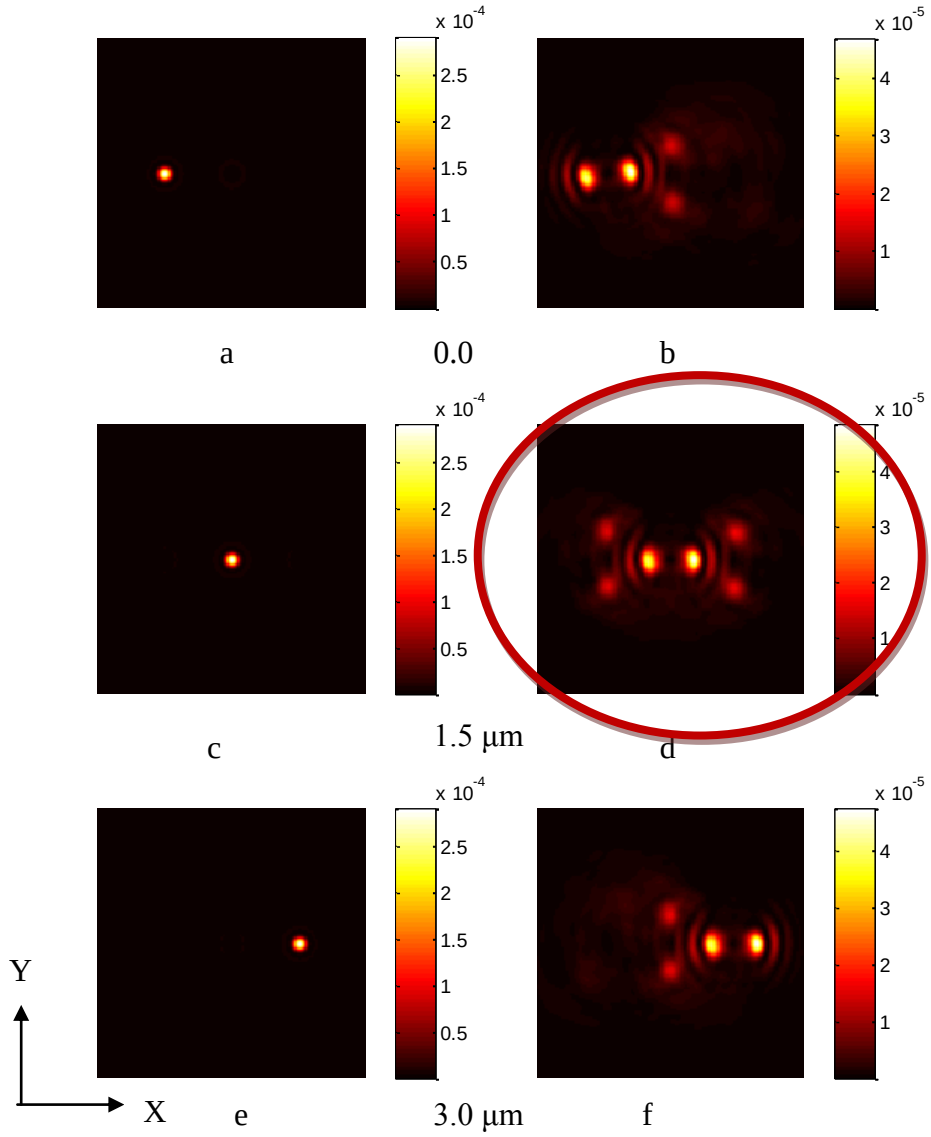

Figure 31. XY View for Images with the 3 bead object for Conventional system (a, c & e) and DH-PSF (b, d & f).

The DH-PSF based system can provide a single image (Figure 31d) from which information about the Z location of the 3 beads can be obtained by mapping rotation angles (Figure 28) to the calibration curve. In contrast, with a conventional PSF system each layer needs to be successively scanned till the best focus for each point source is reached.

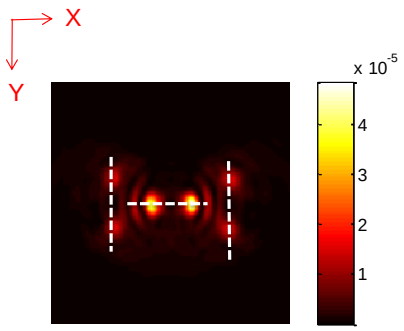

Figure 32. A single DH-PSF based system image can give us information about the entire volume by mapping rotation angle to the calibration curve (Figure 4).

The angle subtended by each of the DH-PSFs is mapped back to calibration curve 1 to get the exact depth.

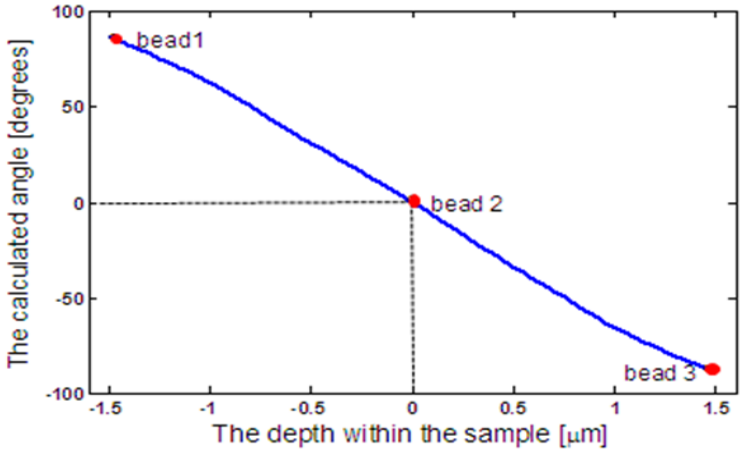

Figure 33. Mapping the angle subtended by the 3 beads to obtain their depths which are empirically determined to be -1.5 μm, 0 μm and 1.5 μm.

The computed angles from the 3 sets of lobes and the corresponding depths obtained from the curve are listed in Table 1 below.

Table 1. Depth obtained from the calibration curve using a single2D image from the DH-PSF system.

Bead number	**Angle subtended to the horizontal axis (in degrees)**	**Location of the bead= (Location of the image + location calculated from calibration curve) [μm]**
1	**86.76**	**1.5 - 1.5=0**
2	**-0.16**	**1.5+0.0=1.5**
3	**-87.01**	**1.5+1.5=3.0**

Since the calibration curve is continuous the accuracy of super localization is only limited by the pixel size. Using a single image at a depth of 1.5 μm depth information about 3 point sources could be obtained using a standard calibration curve. Not only could we determine accurate depth information but also using 1 2D image. We are aware that systems have SA so despite having proof of principle in the above experiment; we need to evaluate the effect of SA on the depth estimation.

5.4.1.2. Images with SA

The depth variant imaging model (Equation 6) was implemented in COSMOS was used to obtain the images. The object thickness of 3.2 μm was divided into 4 strata, and thus 5 PSFs (Figure 10) were required to compute the images (Figure 34 and Figure 35).

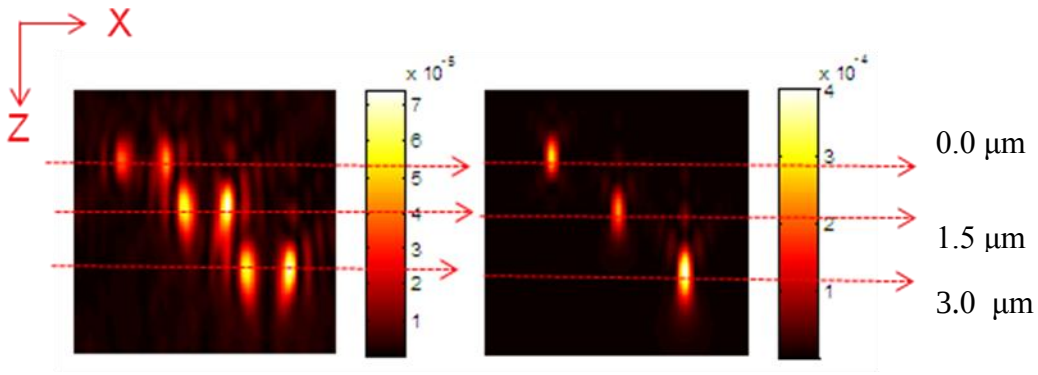

Figure 34. Image with DH-PSF (a) and conventional PSF (b) with SA with the 3 beads.

The image (Figure 34) of the 3 point sources at depths 0.0 μm, 1.5 μm and 3.0 μm look very different structurally due to asymmetry introduced by SA. Again for a conventional system the user needs to scan through multiple planes to get to the planes where the object is located i.e. the image is sharpest but for a DH-PSF based system 1 2D image suffices (Figure 36). Similarly as the earlier experiment only 1 2D image at 1.5 μm was used to obtain depth information about the entire 3D volume.

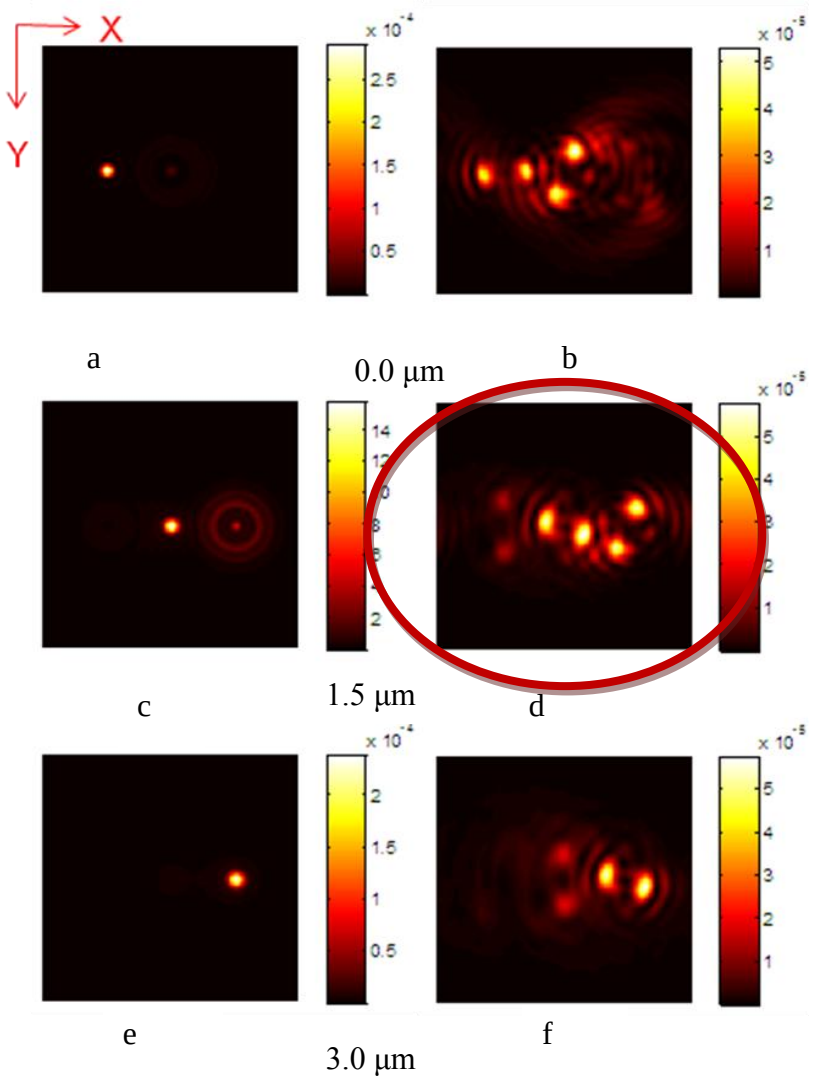

Figure 35. XY View for Images with the 3 bead object for Conventional system (a, c & e) and DH-PSF (b, d & f).

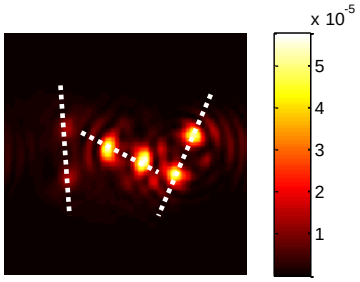

Figure 36.A single DH-PSF based system image used to obtain the depth (Figure 4).

The DH-PSF based system can provide a single image (Figure 35 d, Figure 36) from which information about the Z location of the 3 beads can be obtained. Mapping rotation angle of each bead obtained from Figure 36 to the calibration curve (Figure 37) gives us location which is not true. Due to SA the best focus is shifted, which worsens with greater depths.

Using calibration curve 1 the depth obtained is shown below.

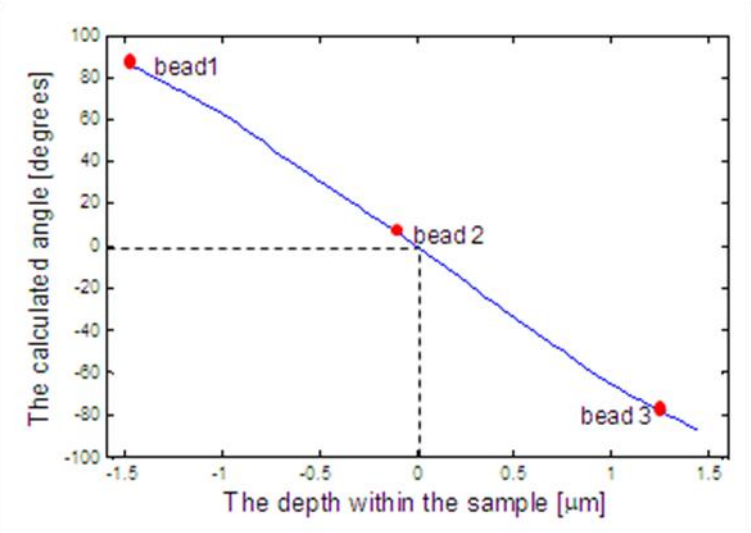

Figure 37. Mapping the angle subtended by the 3 beads to obtain their depths which are empirically determined to be -1.5 µm, - 0.1 µm and 1.3 µm.

Table 2. Depth obtained from the calibration curve using a single image from the DH-PSF system (Figure 35).

Bead number	**Angle subtended to the horizontal axis (in degrees)**	**Location of the bead= (Location of the image + location calculated from calibration curve) [µm]**
1	89.85	1.5-1.5=0
2	6.00	1.5-0.1=1.4
3	-77.95	1.5+1.3=2.7

Since this is incorrect, the second calibration curve (Figure 38) is used to obtain the true depth from the apparent depth.

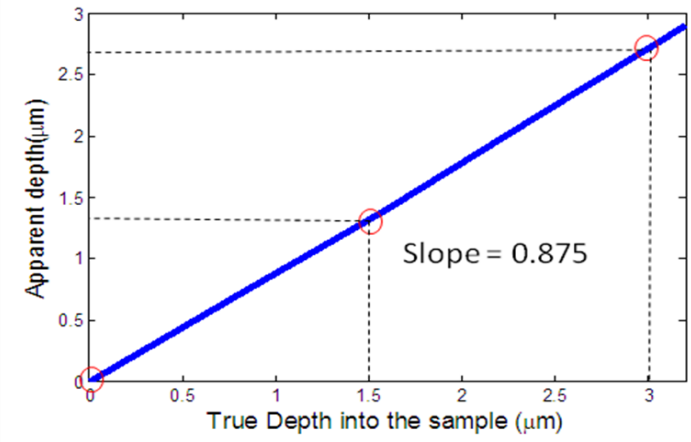

Figure 38. The true depth is obtained as 0.0 µm, 1.5 µm and 3.0 µm from the apparent depths of 0.0 µm, 1.4 µm and 2.8 µm

The second calibration curve maps the previously determined apparent depths to the true depth. Here the true depth is empirically obtained to be 0.0 μm, 1.5 μm and 3.0 μm which correspond to the true depths in our simulated data.

5.4.2. Cylindrical Object

An elongated cylindrical object was simulated for this experiment to observe the effect of DH-PSF based system on elongated objects. Two point sources were used as markers to obtain the length of the cylinder.

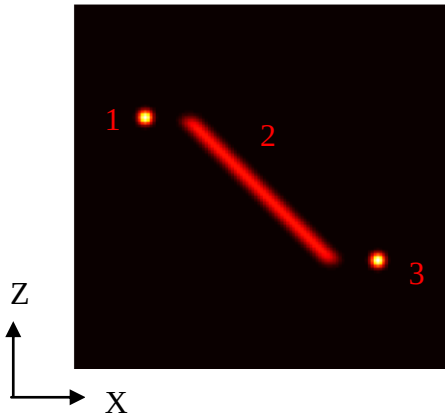

Figure 39. The cylinder object with marker beads.

The cylinder object (Figure 39) comprises of two small spheres 400 nm in diameter located within a watery sample (RI=1.33) at depths of 0 μm and 2.5 μm and the cylinder is 100 nm in diameter and 2.5 μm in length. The object window is taken to be 256x256x256 pixels so that windowing effect can be prevented. Simulated images of this object were generated using for both a DH–PSF based system and a conventional system using PSFs with and without SA. The intensities of the cylinder is kept 10 times lower to the beads since during 3D convolution due the superposition of the lobes the intensity of

the cylinder amplifies so much that the beads become very dim, which in turn poses a problem for the angle estimator algorithm.

5.4.2.1. Images WITHOUT SA

The images are obtained equation 6 with the cylindrical object (Figure 42, Figure 43 and Figure 40) using CosmTools Variant tab.

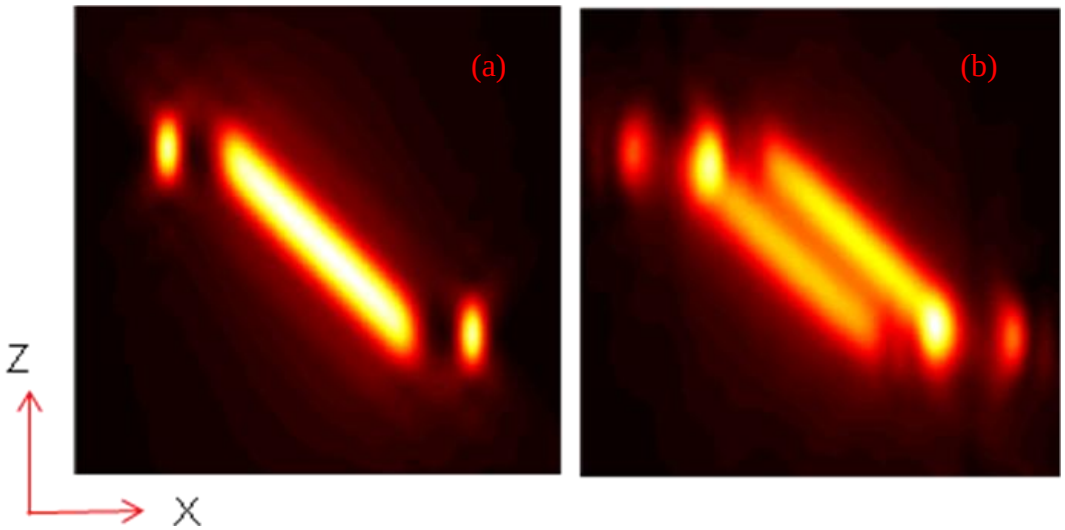

Figure 40. Image with DH-PSF (a) and conventional PSF (b) without SA.

A series of 2D XY cut-views are generated for the conventional system (Figure 41. The XY view of the SI image of the cylindrical object from -2.0 μm -2.0 μm with a conventional system.) and the DH-PSF based image (Figure 42) to see if we can obtain depth from rotation at any specific XY image using just the elongated object. Scanning through the image we could not achieve depth from rotation using a single XY image of the cylindrical object (DH-PSF system) but the two beads acted as markers and hence

allowed us to obtain depth from rotation. An image depth 0.00 µm is chosen (Figure 43) to get the length of the cylinder.

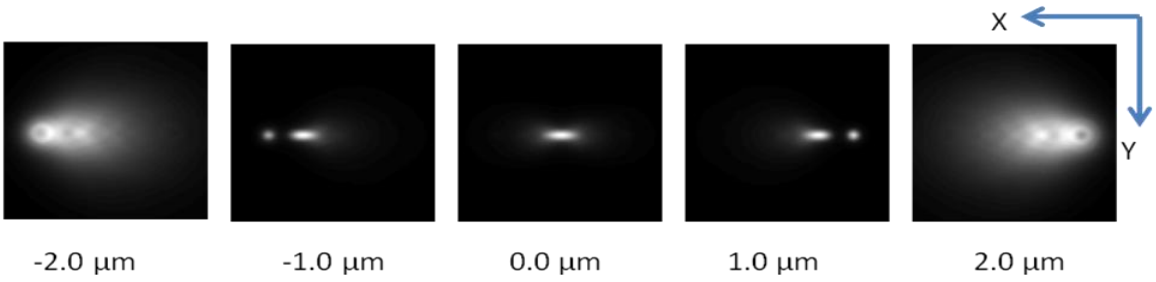

Figure 41. The XY view of the SI image of the cylindrical object from -2.0 µm -2.0 µm with a conventional system.

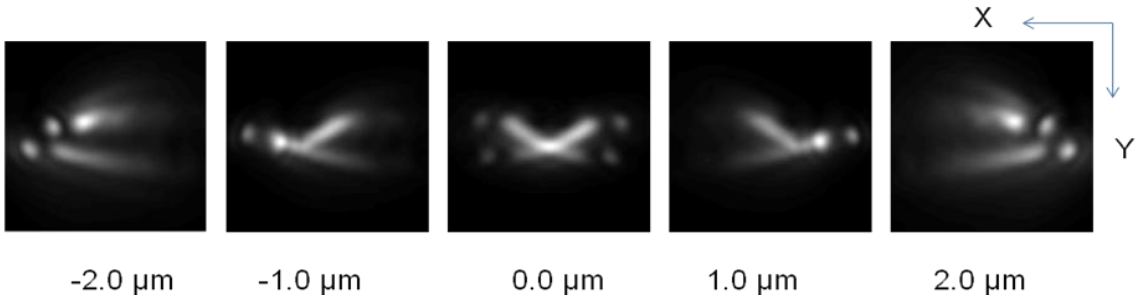

Figure 42 . The XY view of the SI image of the cylindrical object from -2.0 µm -2.0 µm with a DH system.

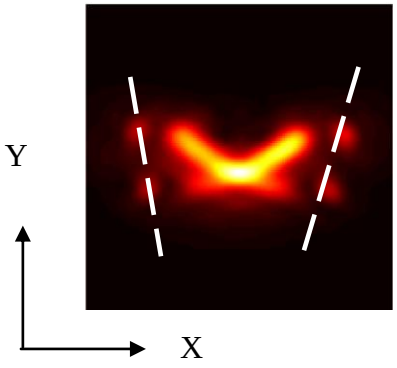

Figure 43. A single DH-PSF based system image used to obtain the depth (Figure 43).

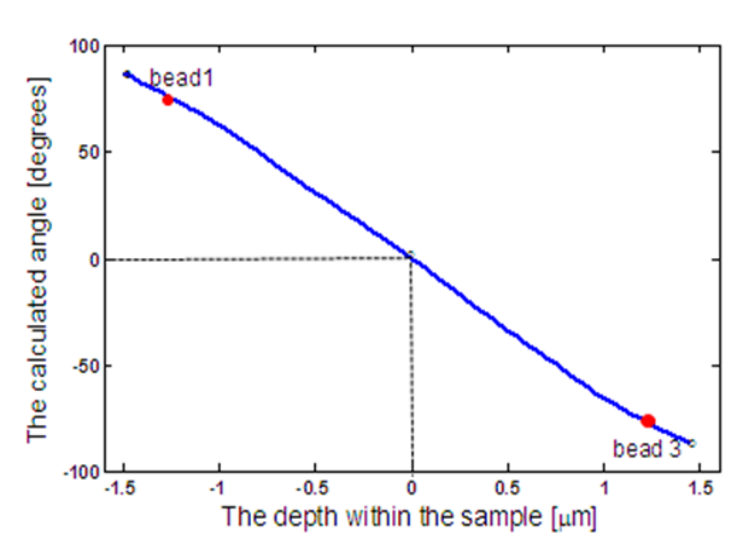

Figure 44. Mapping the angle subtended by the 3 beads to obtain their depths which are empirically determined to be -1.25 μm, and 1.25 μm.

The depth of the markers is obtained from the calibration curve 1 (Figure 4).

Table 3. Depth obtained from the calibration curve using a single image from the DH-PSF system (Figure 43).

Bead Number	**Angle subtended to the horizontal axis (in degrees)**	**Location of the bead= (Location of the image + location calculated from calibration curve) [μm]**
1	75.52	1.25-1.25=0.0
3	-74.23	1.25+1.25=2.5

Using Table 4 the location of each bead is found to be 0.0 μm and 2.5 μm. Using prior knowledge that the beads are located at the edge of the cylinder the total length of the cylinder is 2.5 -0=2.5 μm.

5.4.2.2. Images with SA

Images of the elongated object with SA from both DH-PSF system and conventional system where simulated. The depth variant approach (implemented in COSMOS Tools using the variant tab) was used to generate the images. The distance of 3.2 μm was divided into 4 strata and 5 PSFs (Figure 10) were used to obtain the image (Figure 45). The object space was divided into strata and the 3D PSFs at the location above and below the strata are interpolated to get the 3D PSF valid over the entire strata which are convolved to the strata to get the image of the strata. The superposition of the images of the strata gives the image of the whole sample.

In Figure 45 there appears to be a bending of the cylinder in the conventional system with SA as opposed to no SA systems (Figure 44). With the Dh-PSF system there is an asymmetry along Z, with a shift in the best focus of the system.

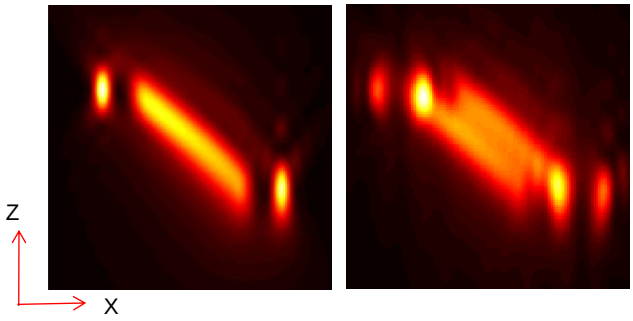

Figure 45. Image with DH-PSF (a) and conventional PSF (b) with SA.

A single 2D image at depth 1.25 μm (Figure 46) is used to obtain the length of the cylinder.

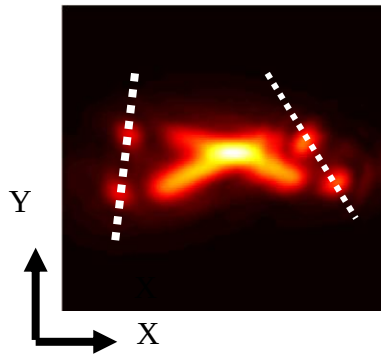

Figure 46. A single DH-PSF based system image used to obtain the depth by mapping angle rotation to the calibration curve (Figure 4).

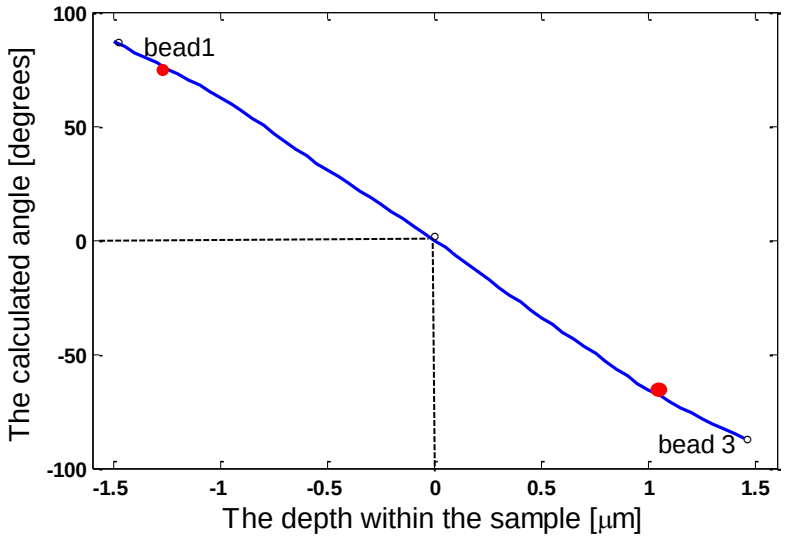

Figure 47. Mapping the angle subtended by the 3 beads to obtain their depths which are empirically determined to be -1.25 μm and 1.10 μm.

Using

Figure 47 the length of the bead is found out to be 2.35 μm, which is not correct hence a second calibration curve (Figure 48) is used to fix the error.

Table 4. Depth obtained from the calibration curve using a single image from the DH-PSF system (Figure 46).

Bead Number	**Angle subtended to the horizontal axis (in degrees)**	**Location of the bead= (Location of the image + location calculated from calibration curve) [µm]**
1	75.52	1.25-1.25=0
3	-65.22	1.25+1.1=2.35

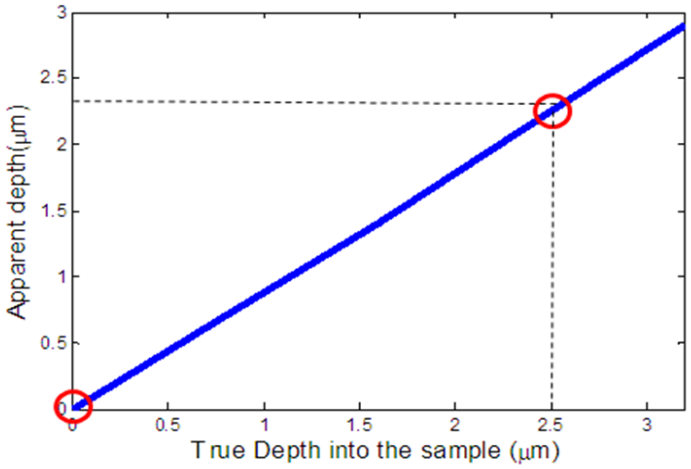

Figure 48. The true depth is obtained as 0.0 µm and 2.5 µm from the apparent depths of 0.0 µm and 2.35 µm

Using Table 4 the location of the beads is obtained as 0.0 µm and 2.35 µm which is again mapped to calibration curve 2 (Figure 48. The true depth is obtained as 0.0 µm and 2.5

μm from the apparent depths of 0.0 μm and 2.35 μm) to obtain the true location of each bead as 0.0 μm and 2.5 μm. The length of the cylinder is obtained from the true depth of the marker beads as 1.25 - 0.0 = 1.25 μm which corroborates with simulated data.

The cylindrical object in the prior experiment was along the XZ direction. We did a second set of experiments with the cylinder oriented along the diagonal of XY and a diameter of 2 pixels, i.e., it's a line along XY. One 2D plane in a 3D volume has this line. We convolved (3D) the line (Figure 49) to the 3D DH-PSF to obtain a series of rotating points. The tip of the cylindrical object image (Figure 50) provides us with rotating points which can be used for calibration. The blue and red circles show the rotation of the tip of the cylinder. This rotation can be mapped to a calibration curve to get the depth object. We can hence conclude that depth from rotation can be obtained using elongated objects provided the elongation is in the XY plane.

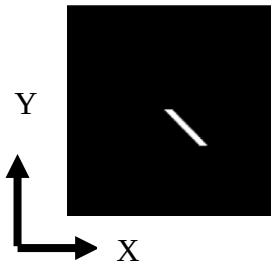

Figure 49: The cylindrical object along XY.

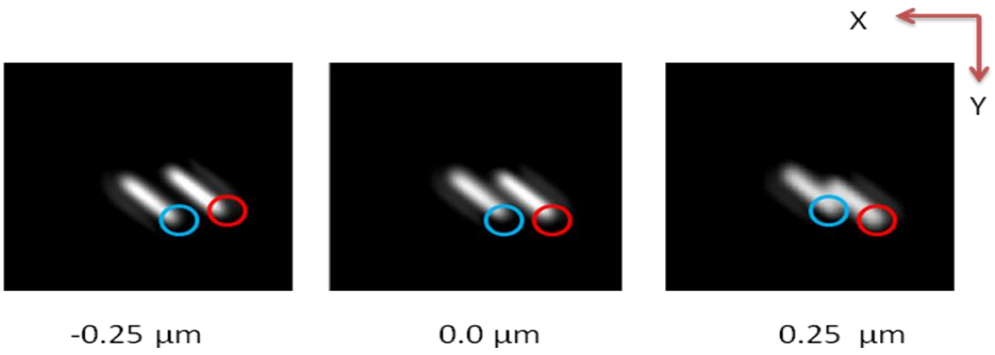

Figure 50. A series of defocused objects exhibiting the effect of DH-PSF on elongated object.

Noise affects the ability of the angle estimation algorithms to obtain the angles of the image since it depends on the intensity .Noise has high intensity values hence the algorithm gets misdirected. But the angles are preserved and improved algorithms can help to extract the angle from noisy images.

6. 3D Intensity Estimation using 3D Images from a DH-PSF System

Images collected from the microscope are generally blurry for traditional systems, and have other types of aberrations. In order to overcome this problem computers are used with algorithms which improve the quality of images to give us the best estimate of the object. With DH-PSF system images there is an additional problem that the image is structurally different from the true object hence this inverse problem becomes additionally significant. In this section 3D intensity estimation algorithms are applied to 3D images of objects 1) fully resolved two beads, 2) under-resolved two beads and 3) elongated object using DH-PSF system and conventional system. Poisson noise is introduced to the images to observe the performance of the EM algorithms. Both the SIEM and the DVEM algorithm were used for non-SA and SA system respectively. The COSMOS Estimation module was used for the 3D intensity estimation.

6.1. Simulated Images

Images of the objects was simulated using a simple convolution [Eq. 5] of the object with the PSFs (DH and conventional). The COSMTools convolution tab was used to generate the images. Using theses image depth estimation was done (Page: 40). The study was extended to SA based systems. The COSMTools variant tab which implements [Equation 6] was used to generate the image with the effect of SA. For the SA system, 4 strata were used in the strata approximation model (Eq. 9) i.e. 5 PSFs were required and computed at depths 0.0 μm, 0.8 μm, 1.6 μm, 2.4 μm, and 3.2 μm (Figure 10).

6.1.1. Noisy Images

In order to study the effect of DH-PSFs on a plethora of imaging condition 2 objects were used 1) the cylindrical object investigated earlier and the 2) two bead object which are separated by 100nm i.e. below the diffraction limit.

We introduce Poisson noise with varying SNR and see the effect on estimation algorithms. Since it's already established that both conventional and DH-PSF based systems are prone to SA the depth variant strata approach is used. The matlab command *imnoise* is used to introduce the noise. The Poisson noise was chosen. This noise function works only on integers hence the intensity was converted to integer value and reconverted to float32 to get the noisy image (Appendix 1).

Poisson noise was chosen since light impinging on the CCD camera follow Poisson statistics. A key feature of Poisson statistics is that the standard deviation is equal to the square-root of the number of individual particles. That is, if there are N particles in each pixel, the mean is equal to N and the standard deviation is equal to $\sqrt{N}$. This makes the signal-to-noise ratio equal to N/$\sqrt{N}$, or simply, $\sqrt{N}$.

$$SNR = \frac{\sum_{k=1}^{K}\sum_{j=1}^{J}\sum_{i=1}^{L}\sqrt{I_{kji}}}{J \times K \times L} \qquad [15]$$

where *J,K,L* are the total number of pixels along the X,Y and Z directions and *I*(*k,j,i*) is the intensity at pixel (*k,j,i*).

6.2. Image Intensity Estimation – Methods

The inverse algorithm was implemented on the image to obtain the estimated objects. The image estimation algorithms SIEM and DVEM (section 3.4) are applied to the simulated images using iterative invariant and iterative variant tabs of the COSMEstimation module (Figure 45). The noisy images were estimated too using the algorithms. All estimations were run over 5000 iterations for non-noisy images and 500 iterations for noisy images. Regularization is available as part of the COSMEstimation module but was not used in this study, fewer iterations were used for comparison purposes.

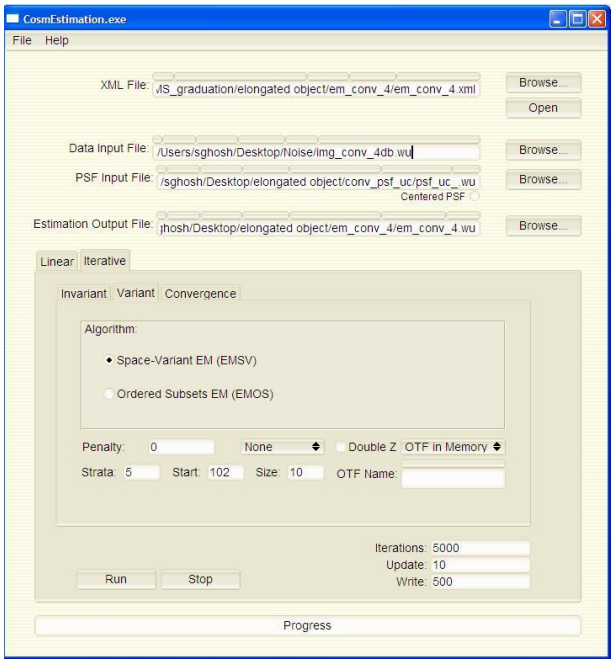

Figure 51. The COSMEstimation module.

6.3. Performance Measures

The quality of the estimated images is determined by the I-Divergence (IDIV) measure. The IDIV measure [37] is defined as

$$IDIV_s = \sum_{i=1}^{m} (s_i \ln \frac{s_i}{\hat{s}_i} + \hat{s}_i - s_i) \quad [16]$$

$\hat{s}_i$ the estimated specimen function and s_i is the true specimen function. The IDIV value is a difference of logs of estimated and true objects. The difference between the estimated and true intensities is not over estimated using this kind of measure. The lower the IDIV value between the estimated image and the true object, the better the quality of the image. IDIV graphs are plotted for all the reconstructed objects.

The IDIV value decreases with the increase in number of iterations and after some point the IDIV starts increasing even with the number of iterations for an image being estimated with particular number of strata.

The cross-sections of the true objects and the estimated objects were compared for similarities too.

6.4. Image Intensity Estimation – Results

6.4.1. Two Bead Object

The simple bead object (Figure 53) consists of two spheres 600 nm in radius separated by 600 nm in the axial direction and 1.6 μm in the lateral direction. The 3D

image of the object used in the simulation has a 50 nm pixel size in all directions and a 256x256x256 pixel grid.

The simulated image for a non-spherically aberrant system (Figure 54) was computed using a single PSF computed at a 0 μm depth. Depth variant imaging is used to simulate the images using the variant tab in COSMTools (Figure 55). The PSFs are updated serially by the system from 0 to strata+1. From the plane where the start of the strata is designated the specimen is divided according to the entry in the *size of strata* field and convolved to corresponding PSFs . Intensity estimation was performed by applying the SIEM [17] and DVEM [16] algorithms is to the simulated images shown in Figure 56 and Figure 57.

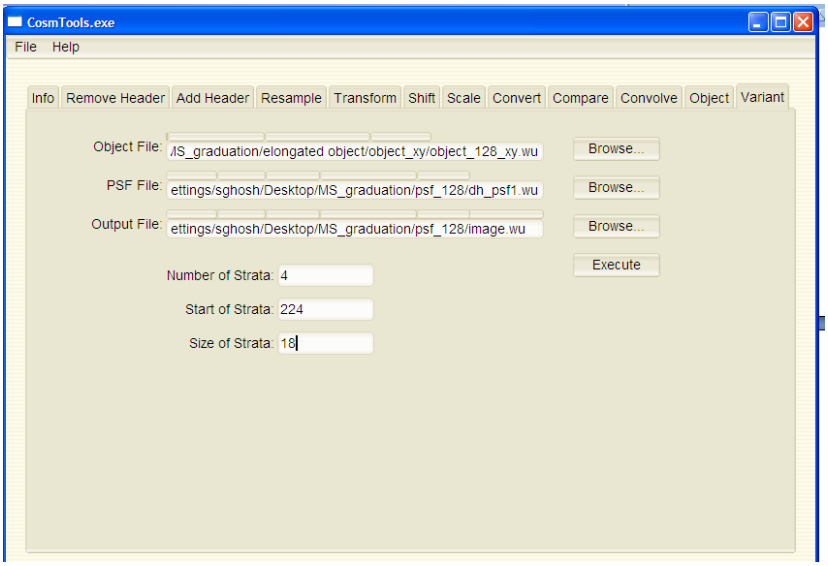

Figure 52. The COSMTools tab with the variant functionality.

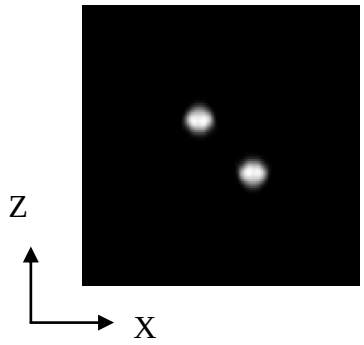

Figure 53. The 2 bead object on a 64x64 XZ view.

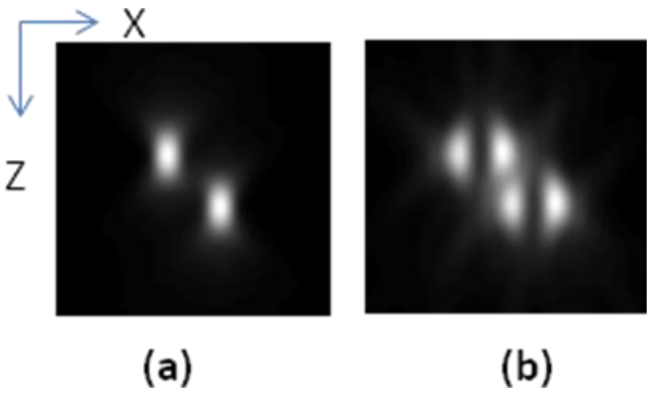

Figure 54. Images with 2 beads object for a non-SA system with Conventional system (b) and DH-PSF based system (b).

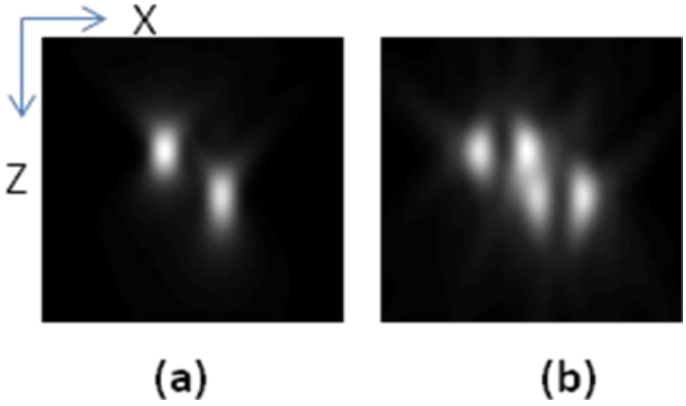

Figure 55. Images with 2 beads object for a SA system with Conventional system (a) and DH-PSF based system (b).

In Figure 54, for a system with no SA the image of the point sources appears alike but in SA systems Figure 55 they appear different with marked asymmetry both in conventional and DH-PSF based systems. This occurs since 1 bead is deeper within the sample than the other hence subjected to more SA. In the display they are on the same intensity scale, the bead exposed to SA is dimmer than the beads without SA.

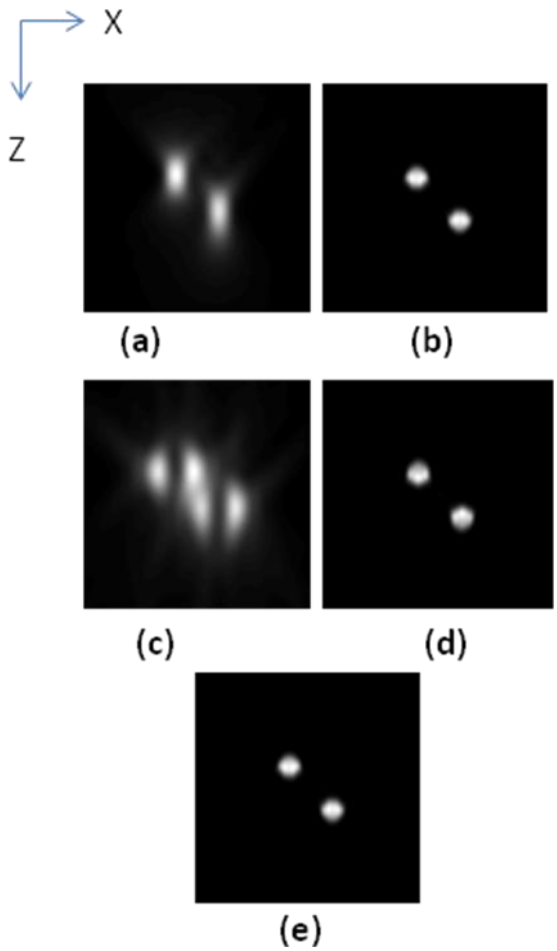

Figure 56. Estimation with SIEM. Image with Conventional PSF (a), estimated object with conventional PSF (b), image with DH- PSF (c), estimated object with DH- PSF (d) and true object (e). XZ view for a 128x128 window. Images are shown on different color scales to aid visualization.

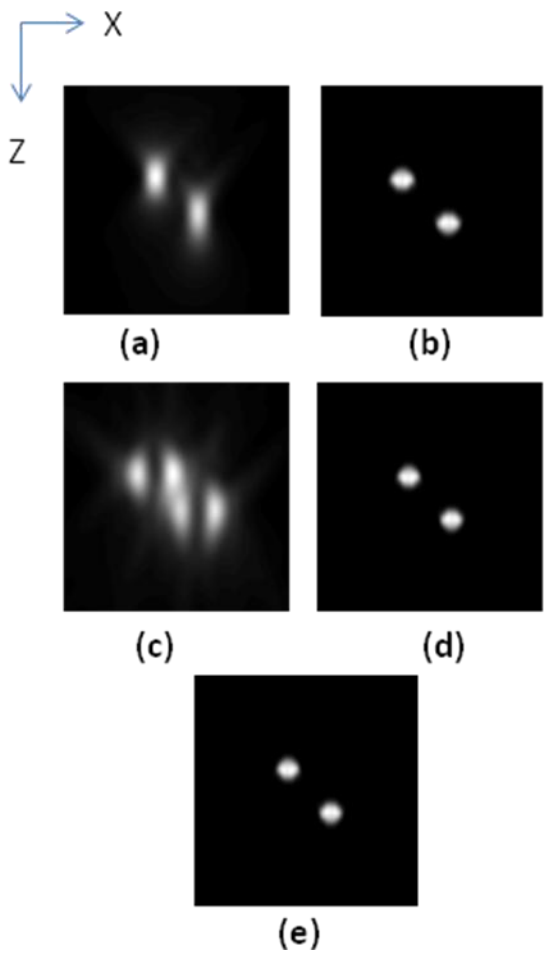

Figure 57. Estimation with DVEM. Image with Conventional PSF (a), estimated object with conventional PSF (b), image with DH- PSF (c), estimated object with DH- PSF (d) and true object (e). XZ view for a 128x128 window. Images are shown on different color scales to aid visualization.

In order to compare the effectiveness of the EM algorithms, the cross-section of the estimated images was compared to the true image (Figure 58) and the I-Divergence was plotted (Figure 59).

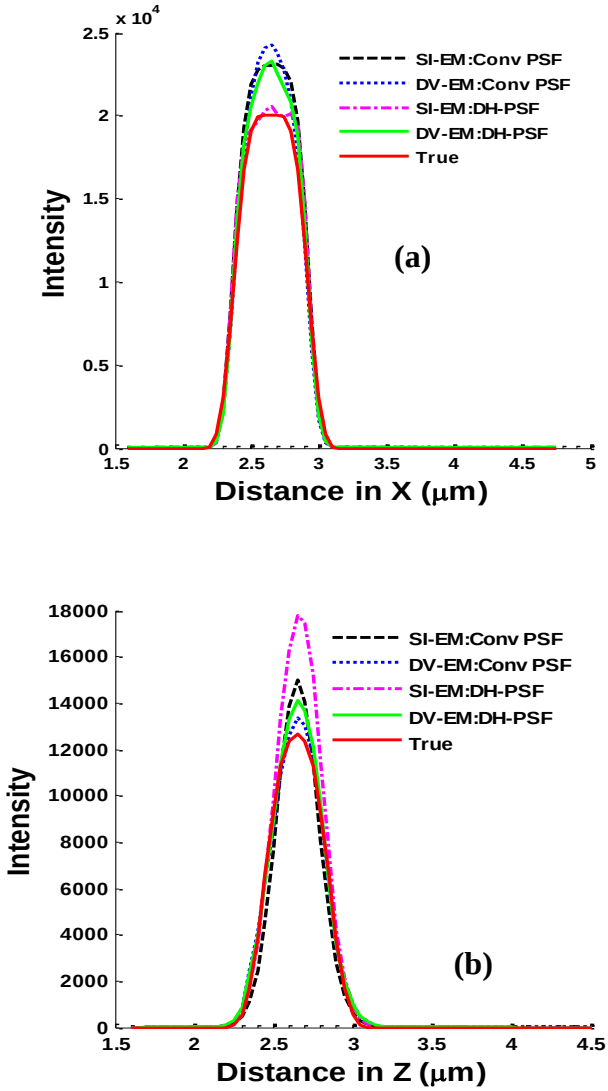

Figure 58. Intensity profile through the center of the XZ images (Figure 56 and Figure 57) along the Z axis (a). Intensity profile through the center of the XY images along the X axis (b).

The relative error along the Z direction for DH-PSF systems are 44% for SIEM systems and 16% for DVEM system while for conventional systems its 20% for SIEM systems and onl;y 4% for DVEM systems. This probably can be attributed to the preservation of the frequenies observed with SA (Figure 58).

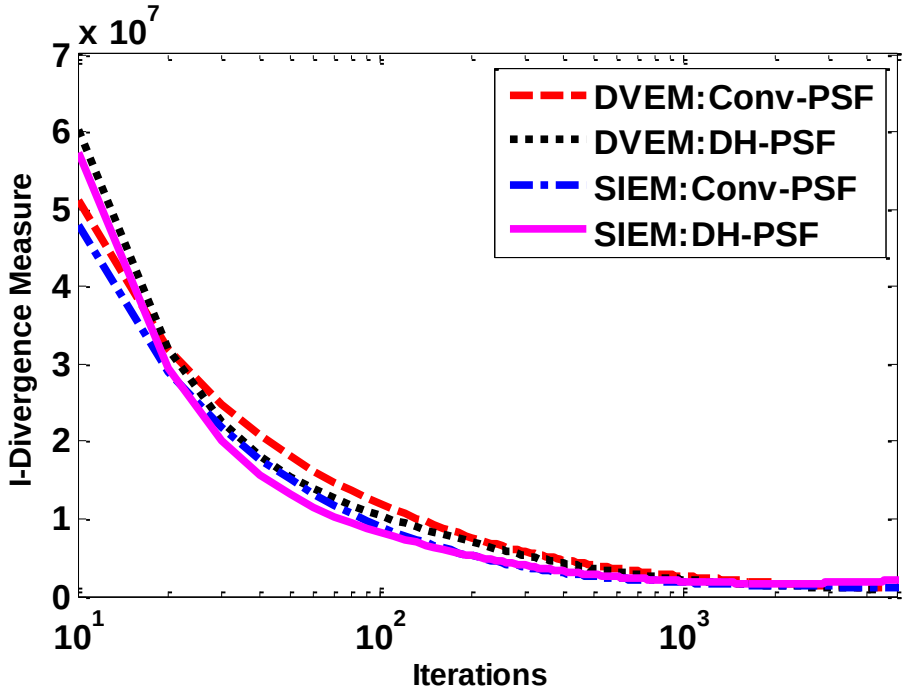

Figure 59. Plot of I-Divergence versus iterations for a system with conventional and DH-PSF for DVEM and SIEM algorithms for 2 bead object.

Looking at the cross sections and the I-Divergence curves (Figure 59) there is good agreement between the performance of SIEM and DVEM algorithms for both the systems, hence we can conclude that the DH-PSF based system do not produce any additional burden to the EM algorithms and can reconstruct the true object.

6.4.2. Under-Resolved 2 Bead Object

Traditionally, the Raleigh resolution limit ($R = \frac{0.61\lambda}{N.A.}$) where λ is the wavelength, has been placed at 275 nm, in this simulation attempts are made to break the

resolution limit. The two bead object (Figure 60) comprises of two small spheres 50nm in diameter located within a watery sample (RI=1.33) 100nm apart axially. The object window is taken to be 256x256x256 pixels with pixel size (50nm) so that windowing effect can be prevented. This object is convolved with PSFs both with and without SA for a DH–PSF based system and conventional system.

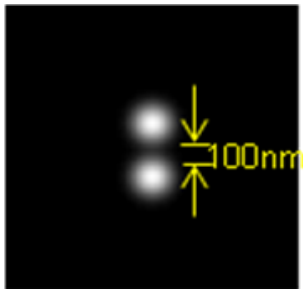

Figure 60. The two bead under-resolved object.

SIEM and DVEM algorithms were run over 5000 iterations for non SA (Figure 61) and SA systems respectively (Figure 62). As evident from (Figure 61 b&d) through the processing with the estimation algorithms super-resolution is achieved as the two beads can be resolved in the estimated result. This is also achieved in the presence of SA (Figure 62 b&d).

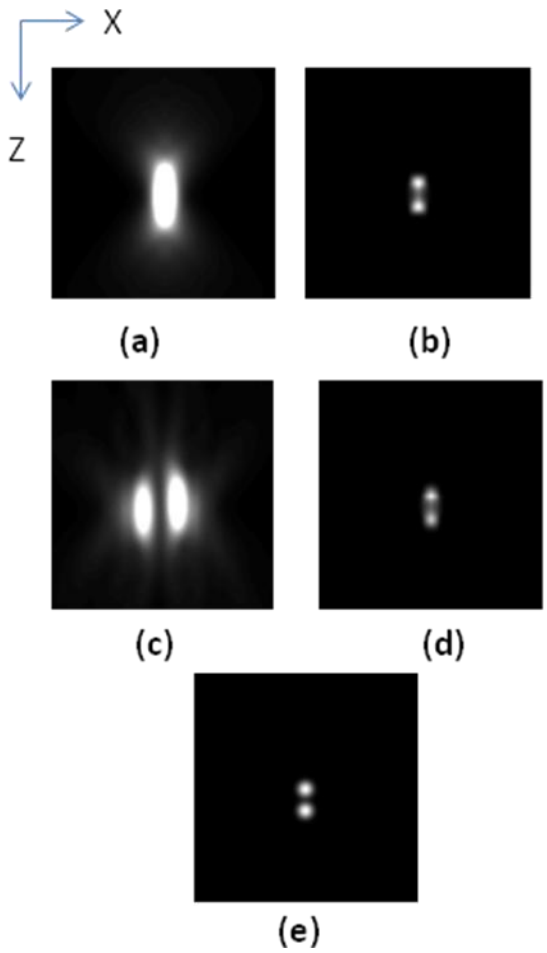

Figure 61. Estimation with SIEM. Image with Conventional PSF (a), estimated object with conventional PSF (b), image with DH- PSF (c), estimated object with DH- PSF (d) and true object (e). XZ view on a 128x128 window. Images are shown on different color scales to aid visualization.

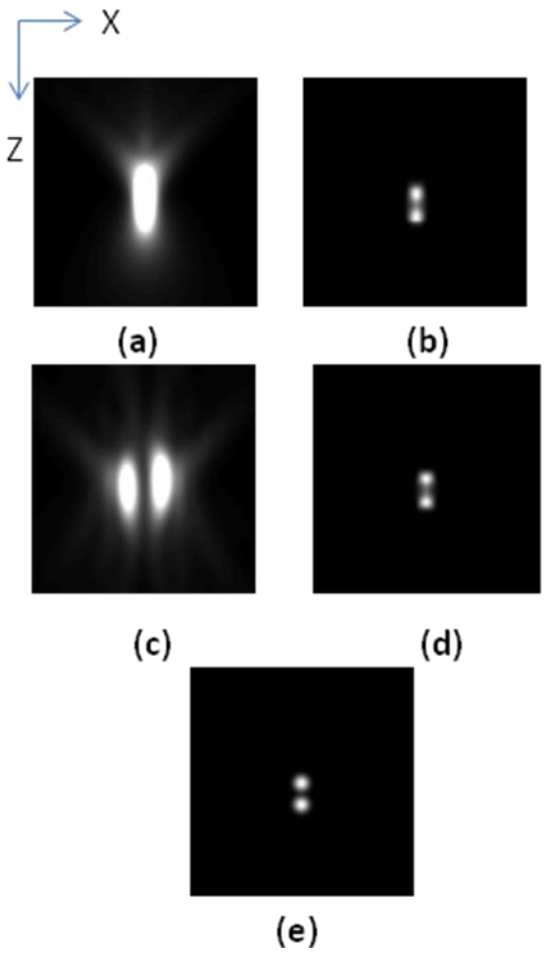

Figure 62. Estimation with DVEM. Image with Conventional PSF (a), estimated object with conventional PSF (b), image with DH- PSF (c), estimated object with DH- PSF (d) and true object (e). XZ view is on a 128x128 window. Images are shown on different color scales to aid visualization.

It's interesting to observe, in the images the two beads are not discernable individually, using the EM algorithms both the beads become partially resolved though not completely resolved like the original object (Figure 61 and Figure 62).

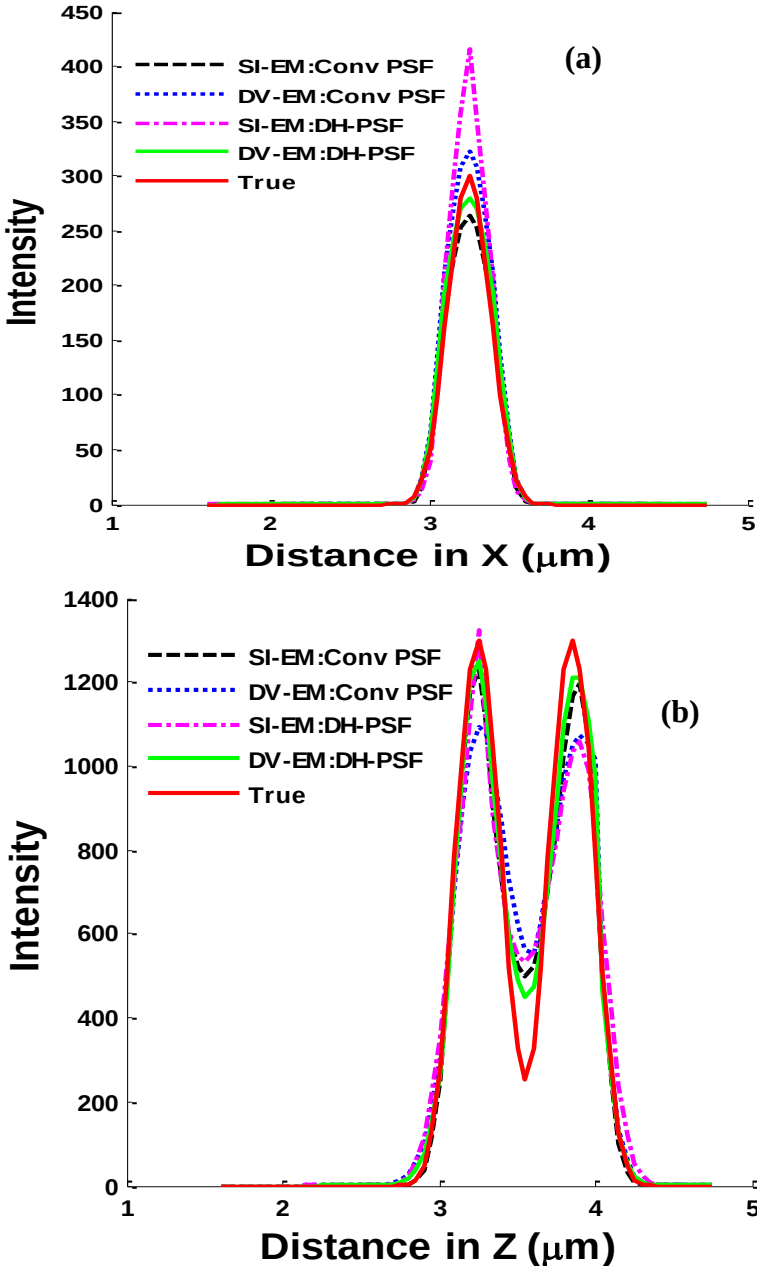

Figure 63. Intensity profile through the center of the XZ images (Figure 56 and Figure 57) along the Z axis (a). Intensity profile through the center of the XY images along the X axis (b).

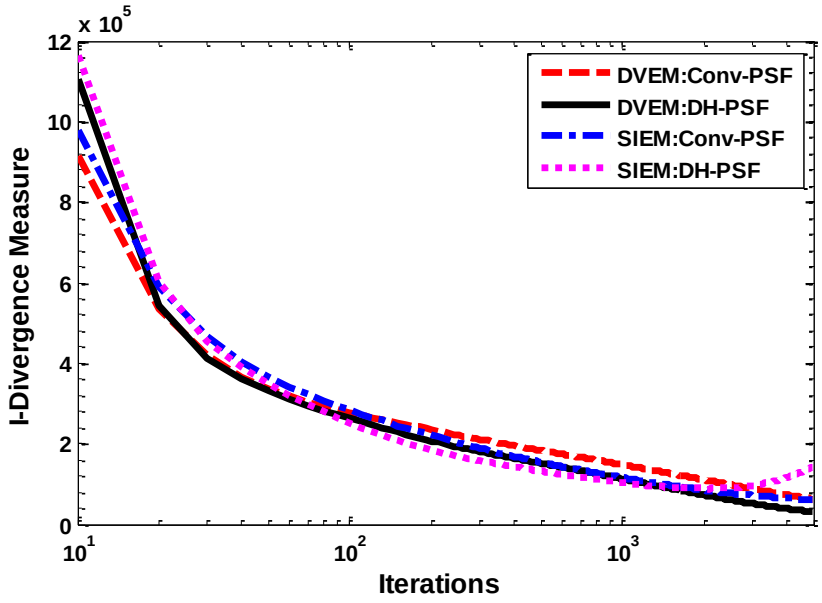

Figure 64. Plot of I-Divergence versus iterations for a system with conventional and DH-PSF for DVEM and SIEM algorithms for under-resolved 2 bead object.

The relative error of the DH-PSF based systems with SA was 9.3% and without SA was 11.5% .With the conventional system it was 7.65% and 10.2% respectively for system with and without SA. The I-Divergence computed using Equation (14) and plotted in Figure 64 shows that the estimated objects come closer to the true object with iterations. The SIEM estimated object with DH-PSF shows divergence after 2000 iteration. The cross-sections through the estimated object intensities (Figure 63) show that the estimated object is well resolved like the true object as opposed to the image where it is under-resolved.

Comparison of the results obtained from the conventional system and the DH-PSF system shows that there is good agreement between the estimated objects by both the systems. Again the loss of symmetry and certain frequencies do not affect the EM algorithms in an adverse way. The DVEM takes into account the effect of SA hence the

estimated object is close to the true object. Depth from rotation cannot be obtained from these objects due to occlusion.

To investigate whether super-resolution is possible in the presence of noise, Poisson noise was introduced the simulated images in (Figure 65). Keeping the object intensity fixed the *imnoise* tab introduced Poisson noise which contributed to SNR values for the conventional system image to be 2.06 dB and for the DH-PSF based system image1.5 dB. The images required to be converted to integer values and back to float32. The noise levels were kept very high to test the effectiveness of the EM algorithms on noisy data. This test was run purely to test the effectiveness of the EM algorithms and not necessarily to provide common ground for comparison between systems hence the SNR was kept dissimilar. Noisy simulations were performed using images with SA (Figure 65) only because depth-varying imaging due to SA is a real problem for both imaging systems and a more challenging inverse imaging problem to solve.

I-Divergence values depends only on intensity values hence with noisy data the I-Divergence curves show erroneous results as to total intensity of a noisy image and a improved image might be the same. Regularization is avoided because it causes loss in resolution. So as a performance measure we compare the cross sections (Figure 66) from estimated object to the true object.

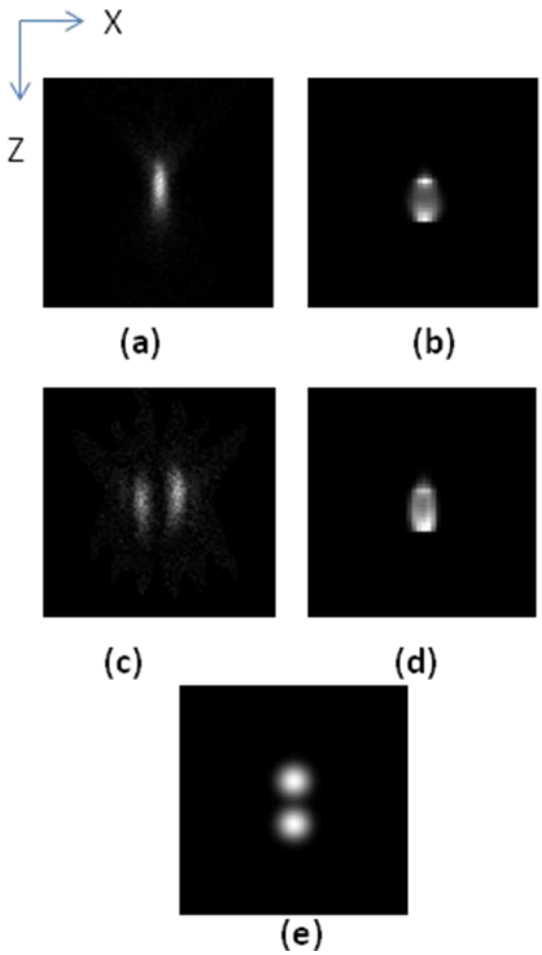

Figure 65. Estimation with DVEM. Image with Conventional PSF with SNR 2.06dB (a), estimated object with conventional PSF (b), image with DH- PSF with SNR 1.5 dB (c), estimated object with DH- PSF (d) and true object (e). XZ view is on a 64x64 window. Images are shown on different color scales to aid visualization.

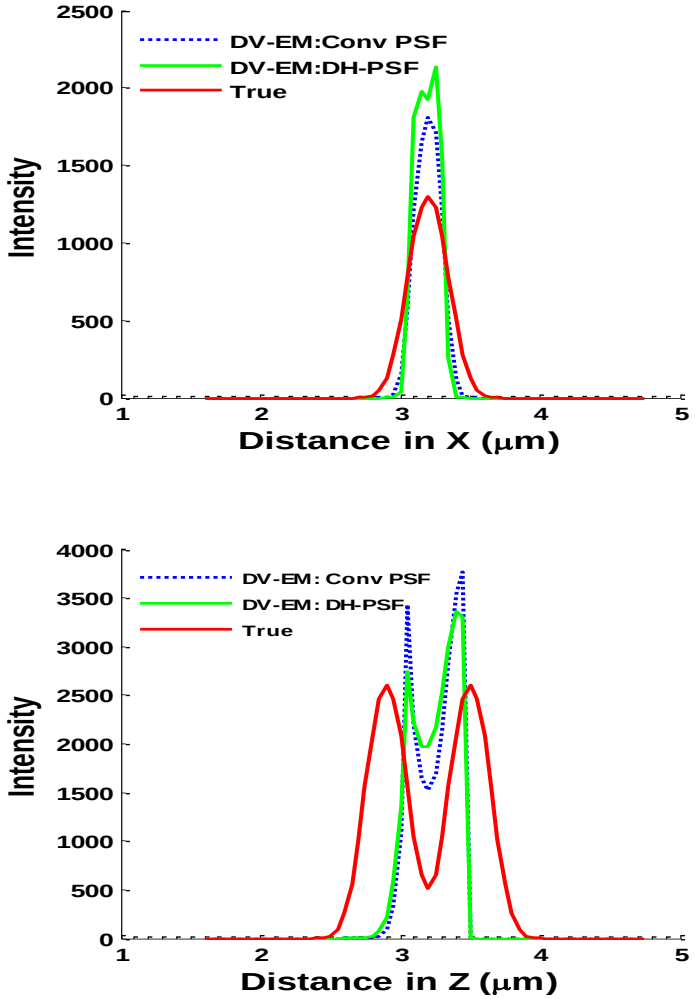

Figure 66. Intensity profile through the center of the XY images (Figure 65) along the X axis (a). Intensity profile through the center of the XZ images along the Z axis (b).

The noise being very high affects the effectiveness of the EM algorithm. The beads are partially resolved as seen from the cross-section (Figure 66) plots but not as good as the resolution without noise. Hence in conclusion, both noisy DH-PSF based images and conventional images can be effectively estimated by using computational algorithms after collecting the images.

6.4.3. Cylindrical Object

The cylindrical object as described earlier was used so that the effect of DH-PSF system on an elongated object as opposed to point sources could be studied. The cylindrical object is used to obtain the images without SA (Figure 43 and Figure 42) and with SA (Figure 45) as described in section (5.4.2). The images are estimated for this study with SIEM (Figure 67) and DVEM algorithms (Figure 68).

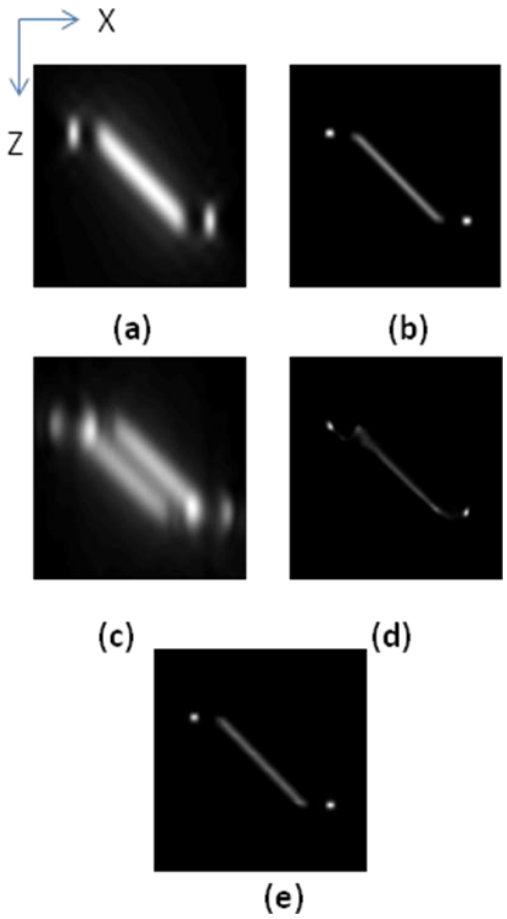

Figure 67. Estimation with SIEM. Image with Conventional PSF (a), estimated object with conventional PSF (b), image with DH- PSF (c), estimated object with DH- PSF (d) and true object (e). XZ view is on a 128x128 window. Images are shown on different color scales to aid visualization.

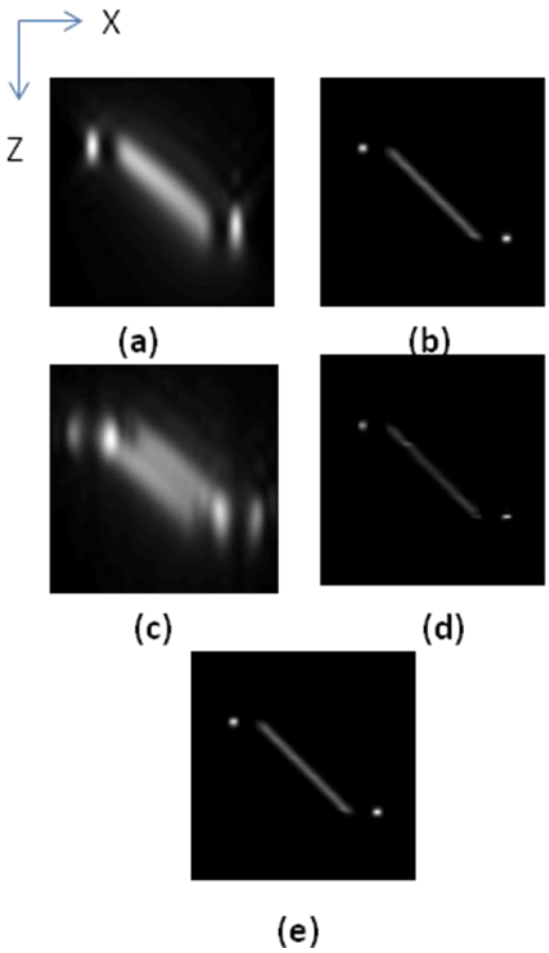

Figure 68. Estimation with DVEM. Image with Conventional PSF (a), estimated object with conventional PSF (b), image with DH- PSF (c), estimated object with DH- PSF (d) and true object (e). XZ view is on a 128x128 window. Images are shown on different color scales to aid visualization.

Looking at Figure 67 and Figure 68 the estimated objects are effectively recovered from the images. There is an aberration in the reconstruction with the DH-PSF both for SI and DV systems which is further seen in the I-Divergence curves (Figure 70).

The I-Divergence (Figure 70) values and cross-sections of the estimated object are compared to the true object to evaluate the algorithm performance (Figure 69). For

this case the cross section profile is taken along the diagonal of the image in the XZ direction so that the profile is more effectively compared.

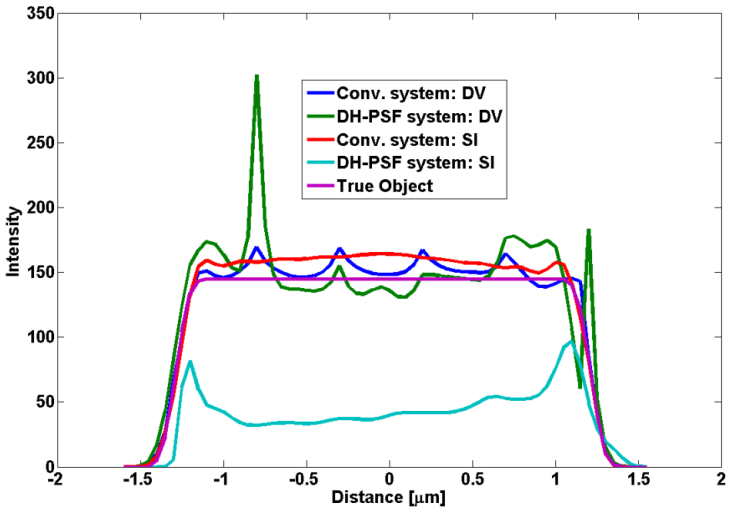

Figure 69. Intensity profile through the diagonal of estimated object (Figure 68 and Figure 68).

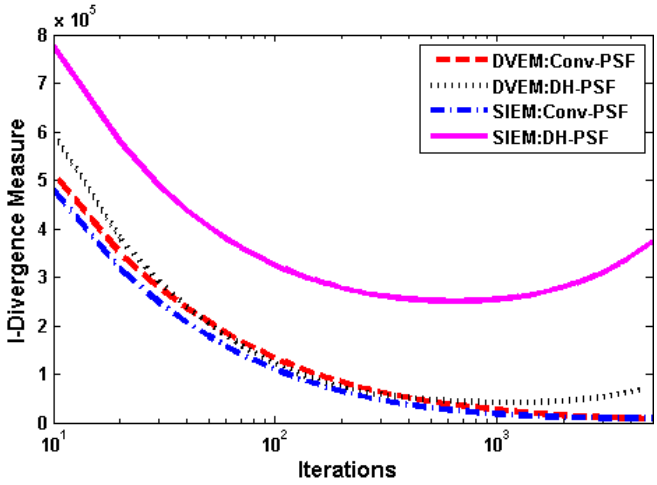

Figure 70. Plot of I-Divergence versus iterations for a system with conventional and DH-PSF for DVEM and SIEM algorithms for elongated cylindrical object.

The SIEM reconstruction with the conventional PSF comes closest to the true object. The DVEM reconstruction shows artifacts with DH-PSFs and also with conventional PSF. It is akin to stratification. Looking at the estimation results it can be clearly noted that the estimation of the DH-PSF based system image with SI-EM is the worst. In an attempt to explain this phenomenon we decided to look at the frequency domain characteristics of the object.

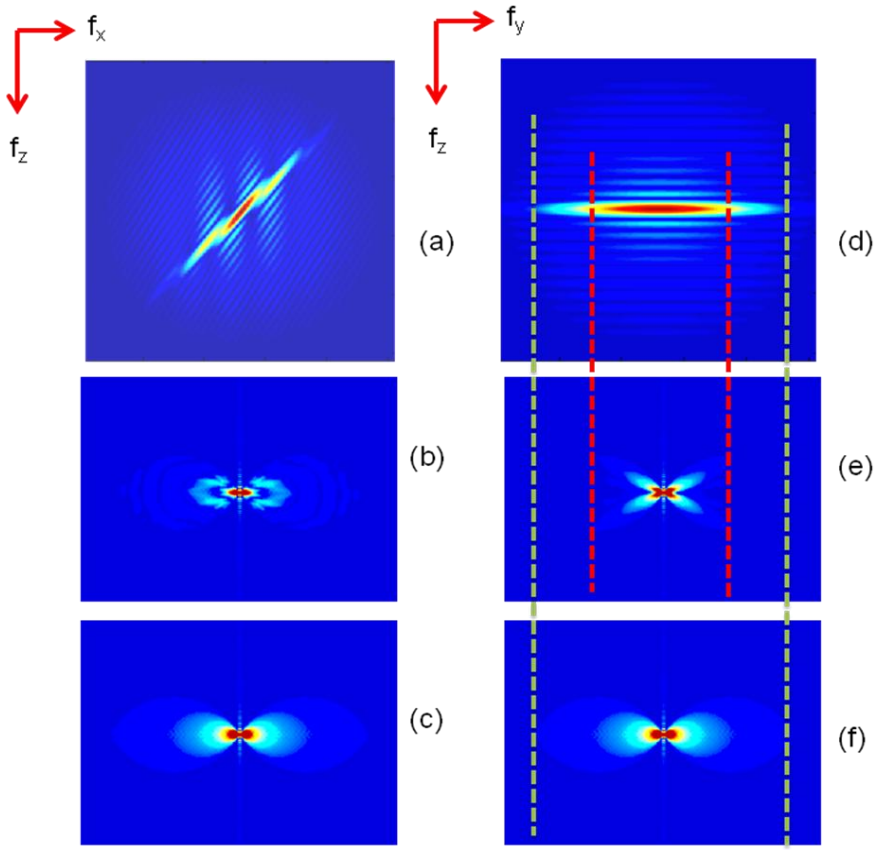

Figure 71. The frequency domain analysis of the cylindrical object. The frequency along $f_x f_z$ of the object (a), DH-MTF (b), Conventional MTF (c) and along $f_y f_z$ of the object (d), DH-MTF (e), Conventional MTF (f).

It can be clearly observed that during convolution in the space domain to create the image, the multiplication in the frequency domain causes loss of some frequencies along f_y which do not occur in the conventional system (indicated by the red and green lines).

The I-Divergence curve for the DH-PSF system estimated with the SIEM system increases due to the aberration creeping in during estimation. The DH-PSF estimation is worse like observed in the under-resolved object. The DVEM results show artifacts for both DH-PSF and conventional PSF based estimation. The DVEM estimated object with DH-PSFs is closer to the true object but still the I-Div curve diverges around 2000 iterations. The observed loss of frequencies in Figure 71 might explain the performance of SIEM estimation using DH-PSFs performing the worst.

Since it already established systems are prone to SA, noisy SA images are studied in the nest section. To make the estimation problem more real, noisy images were calculated using 2 levels of SNR 4 dB and 10 dB (Figure 72). It's run for 500 iterations.

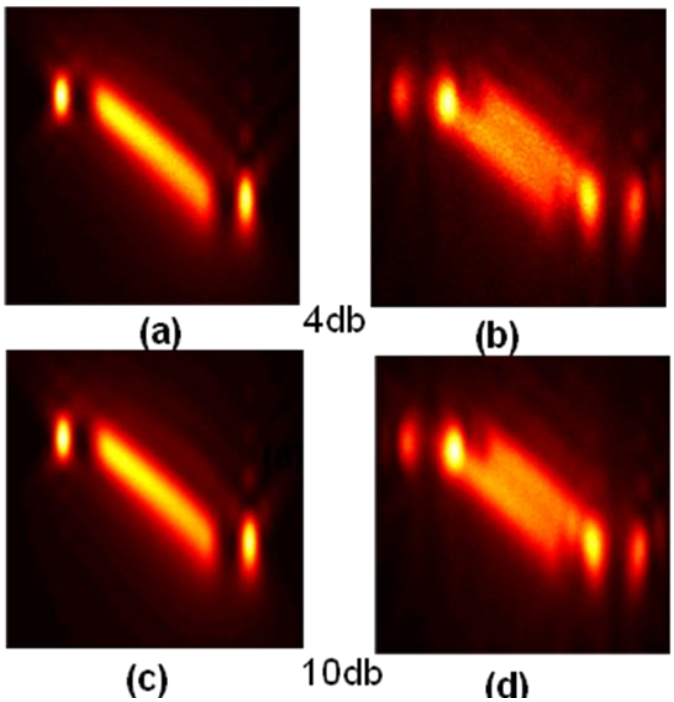

Figure 72. Noisy images for cylindrical object for conventional system (a & c) and DH system (b & d) with noise of SNR 4dB and 10dB.

The DVEM algorithm was applied on the noisy data for 4 dB (Figure 73) and 10dB

(Figure 74).

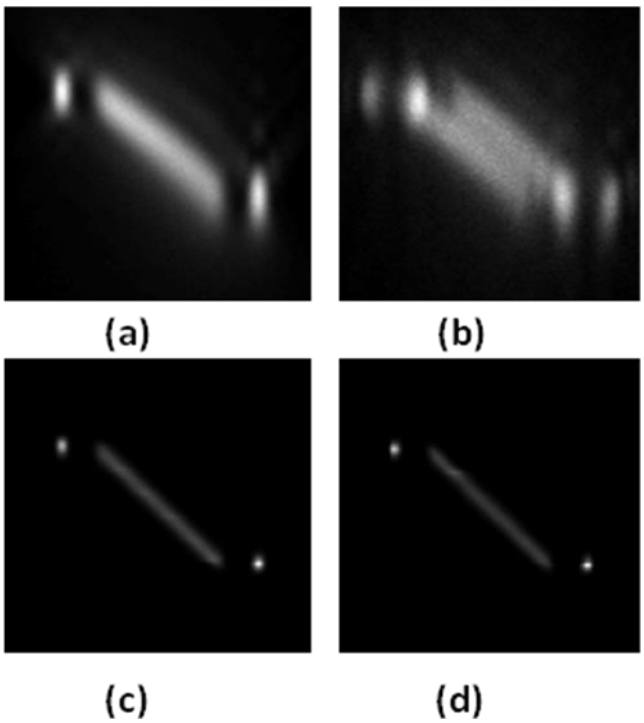

Figure 73. DVEM reconstruction of noisy images with 4dB noise conventional image (a), DH-PSF based system (b), reconstructed object from conventional system (c) and reconstructed object from DH-PSF based system. Images are shown on different color scales to aid visualization.

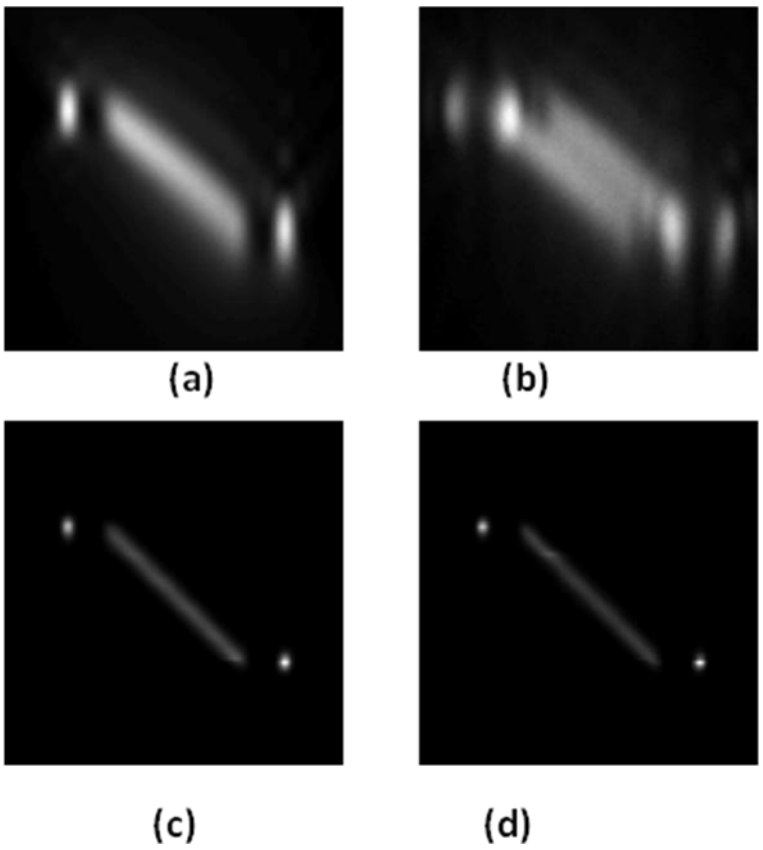

Figure 74. DVEM reconstruction of noisy images with 10dB noise conventional image (a), DH-PSF based system (b), reconstructed object from conventional system (c) and reconstructed object from DH-PSF based system. Images are shown on different color scales to aid visualization.

With the noisy images the EM algorithms perform well in reconstructing the estimated objects even from the noisiest image at 4 dB. In Figure 73 the images with 4 dB SNR show good reconstruction with the conventional PSF and slight aberrations with DH-PSF. Reconstruction with noisy images at 10 dB SNR (Figure 74) also show pretty good agreement with the true object too. The bead objects appear better for the DH-PSF estimation cases.

Regularization would give a better result but since the beads have higher intensity aberrations might creep in. It can be observed that the estimated object with conventional PSF for the 4 dB and 10 dB show good agreement. In this experiment the noiseless estimations show a lot of un-resolved hence its difficult concluding whether the DH-PSF based system has an advantage or not. The DH-PSF based images look worse than conventional images and using estimation algorithms the underlying object can be restored even in noisy cases.

7. Conclusion and Future Work

This thesis provides a method to simulate DH-PSFs using conventional PSFs from a variety of conditions like spherical aberrations. Attempts are made to quantify the effect of spherical aberration on a DH-PSF system. Error correction curves have been introduced to obtain depth from rotation to correct for spherically aberrant system. The DH-PSF based system changes the image considerably from truth and introduces new features into the system; hence the inverse problem is also investigated in this thesis. We introduce EM algorithms applied to DH-PSF based systems which can recreate estimated images which successfully.

In the first chapter the principle of computational optical sectioning microscopy (COSM) was reviewed. 3D imaging is accomplished by successively focusing at varying depths to obtain information about the entire volume of the object. Different types of aberrations in microscopy based system have been discussed with special emphasis on SA. In COSM estimation algorithms are used to improve 3D imaging like the SIEM and DVEM (for spherically aberrant systems) algorithms which use the image obtained from the microscope to get the improved estimation of the true objects. The COSI approach is discussed in detail where the microscope along with a computer contributes to a single entity which brings us to the idea of point spread function engineering. Point spread function engineering involves altering the PSF of a system to gather more information about the system like extended depth of field microscopy and DH-PSF microscopy. DH-

PSFs are discussed in detail, including the computational way developed earlier for the interpretation and estimation of depth from images of a DH-PSF based system.

In the second chapter the genesis of DH-PSF based systems via the implementation of a DH-PSF using SLMs in a 4F microscopy system was reviewed. The use of the DH-PSFs in microscopy was also reviewed.

In the third chapter mathematical models for the DH-PSF, the image formation process and the inverse imaging problem have been presented. In the fourth chapter the computation of the DH-PSF for a system in the presence of SA using a newly developed implementation was discussed in detail. The frequency content of DH-PSFs has been observed with relation to conventional PSFs. It's seen that over the defocus the frequency content is higher in DH-PSFs than conventional PSFs. The DH-PSF shows the missing cone of frequencies consistent with conventional PSF. The 3D DH- MTFs show more information for an SA system which is later justified by the improvement of performance with DVEM algorithms.

In chapter 5 a previously developed depth estimation algorithm was discussed and simulations using the method and images from DH-PSF based system and computer generated objects were presented. It was observed that the SA system shows an apparent shift in the location of the point source which worsens with depth. Corrections were made by introducing a second calibration curve to map the true depth to the apparent depth to get improved localization along Z.

In chapter 6, the 3D image estimation is applied to images from a DH-PSF based COSM. The performance of the estimation algorithms is investigated and compared for

the DH-PSF system and conventional system. Simulations performed using 3 different objects (1) 2 bead object, 2) under-resolved 2 bead object and 3) elongated cylindrical object) were presented. Images were generated using the depth variant and space invariant approach. Depth was estimated using DH-PSF system generated images. The DH-PSF alters the shape of the object hence the inverse problem becomes necessary to be solved. The EM algorithms were applied to the image to get estimated object. To make the simulations a more realistic noise was also introduced in some cases. The EM algorithms worked efficiently on both systems. The EM algorithm was very effective on noisy data. 2 levels of SNR (10db and 4db) were used for the experiments and the EM algorithm was efficient in reconstructing the objects for all 3 cases even without regularization with artifacts. The considerably worse images with DH-PSF based system are recovered using EM algorithms. The DH-PSF system does not provide any specific advantage with estimation. Putting the mask in the system breaks the imaging properties of the system hence recovering the underlying object even with small artifacts is an advantage.

7.1. Contribution of the Thesis

In this thesis DH-PSF based systems have been studied in detail. Software to compute 3D DH-PSFs in the presence of SA was developed by integrating code and phase mask data obtained from the University of Colorado, Boulder. 3D DH-PSFs were computed and the effect of SA was studied. This is the first study of the effect of SA on DH-PSF based systems. The property that in the presence of SA there is a shift in the apparent depth of the point source has been observed for DH-PSF based systems like conventional systems. In this thesis a second calibration curve is introduced which

accounts for this shift introduced due to SA and hence acts as an error correcting mechanism in depth from defocus. EM algorithms have also been applied to 3D simulated images to estimate the true object from the distorted DH-PSF images. This is also the first time that EM algorithms have been applied to DH-PSF systems. The true object can be obtained from the much distorted DH-PSF based system image.

7.2. Future Work

DH-PSF is a very nascent field and a lot of work lies ahead in adapting and using it to different systems. Newer EM algorithms need to be created so that the basic property of DH-PSF is exploited. Looking at the frequency content it may be concluded that fewer images suffice to give information about the whole system. The inverse problem is very important for DH-PSF based systems and to exploit the distinct characteristics of DH-PSFs i.e. the increment in the frequency content over the extent of the DH-PSF.

DH-PSFs have immense applicability in particle tracking, object ranging and super localization which can be applied to fields of biology, physic or chemistry. Using user requirements for customizing the system needs to be done for increasing the applicability of this technology since each area of application comes with its own challenges. DH-PSF is a cutting edge technology that has wide applicability and avenues for research are immense.

References

[1] S. R. P. Pavani and R. Piestun, "Three Dimensional Tracking of Fluorescent Microparticles using a Photon-Limited Double-Helix Response System," Optics Express **16**, 22048-22057 (2008).

[2] J.-A. Conchello and J. W. Lichtman, "Optical sectioning microscopy," Nature review **2**, 920-932 (2005).

[3] P. Sarder and A. Nehorai, "Deconvolution Methods for 3-D Fluorescence Microscopy Images," IEEE Signal Processing, 2006.

[4] T. Cathey and E. Dowski, "New Paradigm for Imaging Systems," in *Applied Optics*, 2002), 6080-6092.

[5] A. Greengard, Y. Y. Schechner, and R. Piestun, "Depth from Diffracted Rotation," in *Optics Letters*, 2006), 181-183.

[6] S. R. P. Pavani, M. A. Thompson, J. S. Biteen, S. J. Lord, N. Liu, R. J. Twieg, R. Piestun, and W. E. Moerner, "Three-dimensional, single-molecule fluorescence imaging beyond the diffraction limit by using a double-helix point spread function," Proceedings Of The National Academy Of Sciences Of The United States Of America **106**, 2995-2999 (2009).

[7] M. A. A. Neil, Juskaitis, and T. Wilson, "Method of Obtaining Optical Sectioning by Using Structured Light in a Conventional Microscope," in *Optics Letters*, 1997), 1905-1907.

[8] S. Hell and W. Wichmann, "Breaking the Diffraction Resolution Limit by Stimulated Emission: Stimulated-Emission-Depletion Fluorescence Microscopy," in *Optics Letters*, 1994), 780-782.

[9] D. B. Murphy, *Fundamentals of Light Microscopy and Electronic Imaging* (Wiley-Liss, 2001).

[10] S. F. Gibson and F. Lanni, "Experimental Test Of An Analytical Model Of Aberration In An Oil-Immersion Objective Lens Used In 3-Dimensional Light-Microscopy," J. Opt. Soc. Am. A-Opt. Image Sci. Vis. **9**, 154-166 (1992).

[11] D. A. Agard, "Optical sectioning microscopy," Annual review biophysics bioengineering, 13:191-219 (1984).

[12] C. Preza, "A Regularized Linear-Reconstruction Method for Optical Sectioning Microscopy," (Washington University, St. Louis, 1990).

[13] C. Preza, M. I. Miller, J. Lewis J. Thomas, and J. G. McNally, "Regularized linear method for reconstruction of three-dimensional microscopic objects from optical sections," Journal of Optical Society of America **9**, 219-228 (1991).

[14] CIRL, "Computational Optical Sectioning Microscopy (COSMOS) ", retrieved (<http://cirl.memphis.edu/comsos>).

[15] C. Preza, M. I. Miller, and J.-A. Conchello, "Image reconstruction for 3-D light microscopy with a regularized linear method incorporating a smoothness prior," Biomedical Image Processing and Biomedical Visualization (1992).

[16] C. Preza and J. A. Conchello, "Depth-Variant Maximum-Likelihood Restoration for Three-Dimensional Fluorescence Microscopy," JOSA-A, 1593-1601 (2004).

[17] J. A. Conchello, "Superresolution and convergence properties of the expectation-maximization algorithm for maximum-likelihood deconvolution of incoherent images," Journal of Optical Society of America **15**, 2609-2619 (1998).

[18] C. Preza and V. Myneni, "3D Reconstruction of Fluorescence Microscopy Image Intensities using Multiple Depth Variant Point Spread Functions," in *BiOS*, (SPIE, 2010), 7570-7572.

[19] T. Mirani, D. Rajan, M. P. Christensen, S. C. Douglas, and S. LWood, "Computational imaging systems: joint design and end-to-end optimality," Applied Optics **47**, B86-B103 (2008).

[20] P. K. Baheti and M. A. Neifeld, "Feature-specific structured imaging," Applied Optics **45**, 7382-7391 (2006).

[21] J. A. O'Sullivan, R. E. Blahut, and D. L. Snyder, "Information-theoretic image formation," IEEE T. Information Theory **44**, 2094-2123 (1998).

[22] A. Greengard, "Three dimensional sensing and imaging using rotating point spread function," (University of Colorado, Boulder, 2006).

[23] D J Brady, A. Dogariu, M. A. Fiddy, and A. Mahalanobis, "Computational optical sensing and imaging: introduction to the feature issue," Appl. Optics, COSI 1-COSI 2, **47**(2008).

[24] S. R. P. Pavani, A. Greengard, and R. Piestun, "Three-dimensional Localization with Nanometer Accuracy using a Detector-Limited Double-Helix Point Spread Function System," Applied Physics Letters **95**(2009).

[25] S. R. P. Pavani and R. Piestun, "3D Fluorescent Particle Tracking with Nanometer Scale Accuracies using a Double-Helix Point Spread Function," Conference On

Lasers And Electro-Optics And Quantum Electronics And Laser Science Conference **1-5**, 1263-1264 (2009).

[26] Y. Y. Schechner, R. Piestun, and S. Shamir, "Wave Propagation with Rotating Intensity Distributions," Physical Review E **54**, R50-R53 (1996).

[27] R. Piestun, Y. Y. Schechner, and J. Shamir, "Propagation -Invariant wave field with finite energy," Journal of Optical Society of America **17**(2000).

[28] S. R. P. Pavani and R. Piestun, "High-Efficiency Rotating Point Spread Functions," Optics Express **16**, 3484-3489 (2008).

[29] G. Sharma, S. R. P. Pavani, and R. Piestun, "Optimization of double-helix point spread function for photon-limited 3D imaging systems," in *COSI*, 2009),

[30] S. Chaudhuri and A. N. Rajagopalan, *Depth from Defocus: A Real Apperture Imaging Approach* (Springer-Verlag, New York).

[31] S. R. P. Pavani, J. G. DeLuca, and R. Piestun, "Polarization Sensitive, Three-dimensional, Single-molecule Imaging of Cells with a Double-Helix System," Optics Express **17**, 19644-19655 (2009).

[32] M. Badieirostami, M. D. Lew, M. A. Thompson, and W. E. Moerner, "Three-dimensional localization precision of the double-helix point spread function versus astigmatism and biplane," Applied Physics Letters **97**.

[33] M. D. Lew, M. A. Thompson, M. Badieirostami, and W. E. Moerner, "In vivo Three-Dimensional Superresolution Fluorescence Tracking using a Double-Helix Point Spread Function," in *Single Molecule Spectroscopy And Imaging Iii* (Spie-Int Soc Optical Engineering, Bellingham).

[34] S. J. Lord, H. L. D. Lee, R. Samuel, R. Weber, N. Liu, N. R. Conley, M. A. Thompson, R. J. Twieg, and W. E. Moerner, "Azido Push-Pull Fluorogens Photoactivate to Produce Bright Fluorescent Labels," J. Phys. Chem. B **114**, 14157-14167.

[35] J. Goodman, *Introduction to Fourier Optics*, 3 ed. (Roberts & Company Publishers, 2005), p. 491 pages.

[36] O. Haeberle, "Focusing of light through a stratified medium: a practical approach for computing microscope point spread functions. Part I: Conventional microscopy," Opt. Commun. **216**, 55-63 (2003).

[37] I. Csiszar, "Why least squares and maximum entropy?An axiomatic approach to inference for linear inverse problems," Annals of Statistics **19**, 2032-2066 (1991).

Appendix

Code for generation of DH-PSF from Conventional PSFs obtained from the COSMOS PSF module using Matlab.

```
%the script runs program that is used to to generate a series of DH-PSF
%from a series of Conventional-PSFs the real and imaginary
%parts

clear all;
close all;
 N =511;
NA= 1.4;
lambda=633;
fc=NA/lambda;
pixel = 50;
apdia=2*(round(fc*N*pixel));              %calculating the aperture
diameter
 load mask.mat

a=mask;

maskcrop= a(35:220,35:220);             %removing the padding
msize=apdia;
mask2=imresize( maskcrop,[msize,msize],'nearest'); %resizing the mask
based on the pupil.
clear maskcrop;
clear a;
clear mask;

for m1=1:5;

a11=WURead3D(['C:\Documents and
Settings\sghosh\Desktop\bios_results\3rd\conv_psf_256\p',num2str(m1),'_
im.wu']);
b11=WURead3D(['C:\Documents and
Settings\sghosh\Desktop\bios_results\3rd\conv_psf_256\conv_psf_uc',num2
str(m1),'_re.wu']);
if m1==0
for m=1:128
c1(:,:,m) =(b11(:,:,m) - (1i*a11(:,:,m)));              % obtaining the
PSF from the real and imaginary parts
end
for m=129:256
c1(:,:,m) =(b11(:,:,m) +(1i*a11(:,:,m)));
end
else

for m=1
```

```
c1(:,:,m) = (b11(:,:,m) - (1i*a11(:,:,m)));
 end
for m=2:256
 c1(:,:,m) = (b11(:,:,m) +(1i*a11(:,:,m)));
end
end
clear a11;
clear b11;
for i1=1:256
N=511;
Npsf=256;
Npad = (N-1-Npsf)/2;
centerit = @(M,N) padarray(padarray(M,[1 1],'pre'),[Npad Npad],'both');

kl = c1(:,:,i1);
cen= fftshift((fft2(fftshift(centerit(kl,N)))));

Npsf=msize;
Npad = (N-1-Npsf)/2;
centerit = @(M,N) padarray(padarray(M,[1 1],'pre'),[Npad Npad],'both');
q =centerit(mask2, N);
k=(ifftshift(ifft2(ifftshift(cen.*q))));
clear q;
clear cen;
clear kl;
pk = k(129:384,129:384);
clear k;
dh_psf(:,:,(i1))=pk';
clear pk;
end
end
clear k;
clear pk;
dis=[8,39,70,101,132,163,194];
clear c11;
clear mask2;
crp=abs(dh_psf).^2;
clear dh_psf;
sum_tot=sum(sum(sum(crp)));
rn= (crp/sum_tot);
clear crp;
cd = sum(sum(sum(rn)))                % setting all the photons of the
system to add up to 1
figure
conv=[c1(:,:,dis(1)),c1(:,:,dis(2)),c1(:,:,dis(3)),c1(:,:,dis(4)),c1(:,
:,dis(5)),c1(:,:,dis(6)),c1(:,:,dis(7))];
imagesc(abs(conv).^2);
axis off;
axis image;
set(gca,'YDir','normal');
colorbar;
title([num2str(((-51+(dis(m)))*0.05)),'\mum'])
figure
dh=[rn(:,:,dis(1)),rn(:,:,dis(2)),rn(:,:,dis(3)),rn(:,:,dis(4)),rn(:,:,
dis(5)),rn(:,:,dis(6)),rn(:,:,dis(7))];
imagesc(dh);
```

```
axis off;
axis image;
set(gca,'YDir','normal');
colorbar;



dr= fopen(['dh_psf_',num2str(m1)],'w+');
dr1=fwrite(dr,rn,'float32');
```

Code for generation of noisy images using Matlab

```
% code to obtain the noisy image from DV images
clc;
close all;
clear all;
img_dv_conv=WURead3D('C:\Documents and
Settings\sghosh\Desktop\MS_graduation\elongated object\im_conv_dv.wu');
%reading the conv. image file
for m=1:256

    b(:,:,m)=imnoise(uint16(img_dv_conv(:,:,m)),'poisson');
%adding the poisson noise

end
 SNR_conv=SNR_poi(b)                          %obtaining the SNR

dr= fopen('img_conv_noise','w+');        %saving the image file
dr2=fwrite(dr,b,'float32');
figure;
imagesc(squeeze(b(64:191,129,64:191))');  %displaying the image
colormap('gray')
%SNR_conv=SNR_poi(b)
clear all ;
 img_dv_dh=WURead3D('C:\Documents and
Settings\sghosh\Desktop\MS_graduation\elongated
object\im_dh_dv.wu');%reading the conv. image file

for m=1:256
    b1(:,:,m)=imnoise(uint16(401*img_dv_dh(:,:,m)),'poisson');  %adding
the poisson noise, an integer factor is added to keep the SNR same

end
SNR_dh=SNR_poi(b1)
%b1=padarray(b1,[64,64,64]);
dr= fopen('img_dh_noise','w+');
dr1=fwrite(dr,b1,'float32');
figure
imagesc(squeeze(b1(:,129,:)));      % display the image
colormap('gray')
```